CROSS SECTIONS FOR PLANETARY SYSTEMS INTERACTING WITH PASSING STARS AND BINARIES

Gongjie Li[1] and Fred C. Adams[2,3]

[1]*Harvard-Smithsonian Center for Astrophysics*
Institute for Theory and Computation, 60 Garden Street, Cambridge, MA 02138

[2]*Physics Department, University of Michigan, Ann Arbor, MI 48109*

[3]*Astronomy Department, University of Michigan, Ann Arbor, MI 48109*

ABSTRACT

Most planetary systems are formed within stellar clusters, and these environments can shape their properties. This paper considers scattering encounters between solar systems and passing cluster members, and calculates the corresponding interaction cross sections. The target solar systems are generally assumed to have four giant planets, with a variety of starting states, including circular orbits with the semimajor axes of our planets, a more compact configuration, an ultra-compact state with multiple mean motion resonances, and systems with massive planets. We then consider the effects of varying the cluster velocity dispersion, single stars versus binaries, different stellar host masses, and finite starting eccentricities of the planetary orbits. For each state of the initial system, we perform an ensemble of numerical scattering experiments and determine the cross sections for eccentricity increase, inclination angle increase, planet ejection, and capture. This paper reports results from over 2 million individual scattering simulations. Using supporting analytic considerations, and fitting functions to the numerical results, we find a universal formula that gives the cross sections as a function of stellar host mass, cluster velocity dispersion, starting planetary orbital radius, and final eccentricity. The resulting cross sections can be used in a wide variety of applications. As one example, we revisit constraints on the birth aggregate of our Solar System due to dynamical scattering and find $N \lesssim 10^4$ (consistent with previous estimates).

Subject headings: planets and satellites: dynamical evolution and stability – planetary systems

1.   Introduction

A large fraction of planetary systems form within stellar clusters (Lada & Lada 2003; Porras et al. 2003) and these birth environments can influence their resulting properties (e.g., see the reviews of Adams 2010; Pfalzner 2013). One potentially important process occurs when binary systems — and single stars — fly past solar systems and disrupt the orbits of their constituent planets. This type of scattering interaction has been studied in the field (Laughlin & Adams 2000), and within young embedded clusters (e.g., Adams et al. 2006; Malmberg et al. 2007, 2011; Boley et al. 2012; Dukes & Krumholz 2012; Chatterjee et al. 2012; Hao et al. 2013; Pacucci et al. 2013), where the latter results can be used to provide constraints on the possible birth environment of our own solar system (e.g., Adams & Laughlin 2001; Williams & Gaidos 2007; Spurzem et al. 2009; Portegies Zwart 2009; Adams 2010; Williams 2010; Pfalzner 2013). We stress that the dynamical constraints derived for the birth aggregate of the solar system depend on many variables, including assumptions made about the cluster properties, any other constraints imposed on the problem, and the interaction cross sections.

This present study focuses on the cross sections themselves, and expands previous work to include a much wider range of parameter space; the implications for the solar birth environment are then briefly considered at the end of the paper. For studies concerning our solar system, most previous work has calculated the cross sections for this mode of disruption by considering the initial orbits of the giant planets to have their present-day values of semimajor axis. However, some recent work suggests that our solar system may have begun in a more compact configuration (Gomes et al. 2005; Tsiganis et al. 2005), and the planets may not have reached their present-day orbits until the solar system reached an age of hundreds of millions of years. One motivation for this present study is thus to determine cross sections for solar system disruption for more compact configurations. Note that the sign of the effect is not obvious *a priori*: The geometrical cross section of the compact solar system is smaller, and hence implies a smaller interaction cross section. However, the decreased relative separations of the planets allow for increased planet-planet interactions, which could result in more disruption from the passing stars; in addition, the close spacing in compact solar systems allows for orbit crossing to occur for smaller values of eccentricity.

In some compact configurations of the solar system, the giant planets can be at or near mean motion resonance. This possibility leads to interesting dynamics: Mean motion resonances can protect planetary systems from disruption, and could thus lead to greater stability and smaller interaction cross sections. On the other hand, the mean motion resonances themselves are more easily compromised than planetary orbits — the potential energy corresponding to the resonance angle being in a bound state is much less than the gravita-

tional potential energy of the planetary orbit. An important related question is thus to find the cross sections for passing stars (including binaries) to disrupt mean motion resonances. Planetary systems with disrupted resonances will usually retain their planets in the near term, although they could be subject to orbit instabilities over longer spans of time.

In addition to compact solar system architectures, this paper considers a wider range of parameter space than previous studies. Part of this expanded scope is possible due to increased computational capabilities. This present study includes results from more than 2 million individual numerical experiments that simulate a solar system interacting with a passing binary (or single star). For each choice of solar system architecture and each choice of the background parameters for the encounters, we run a large ensemble of $\mathcal{N}_E$ simulations (where $\mathcal{N}_E = 80,000$ for most cases, but can be larger). The variations that we consider for the target solar systems include compact configurations (described above), more massive planets, nonzero initial orbital eccentricities, and a range of masses for the central stars. For variations in the background environment, we consider two main issues: the effects of varying velocity dispersion of the cluster and the relative sizes of the interaction cross sections for single stars versus binaries.

This paper is organized as follows. We formulate our approach to calculating the interaction cross sections in Section 2. The resulting cross sections are then given in Section 3, which provides $\langle \sigma \rangle$ for increases in eccentricity, increases in the spread of inclination angles, planet ejection, planet capture, and changes in semimajor axes. Results are also presented for increasing orbital eccentricities up to orbit-crossing configurations and compares the efficacy of passing single and binary stars. These results are given as a function of solar system architecture, velocity dispersion of the cluster, and mass of the host star. Over much of the parameter space of interest, the cross sections display a nearly self-similar form. Section 4 presents a scaling analysis that shows how the results scale with velocity disperion, stellar mass, and starting semimajor axis. As an application, Section 5 revisits the possibile dynamical constraints on the birth cluster of the solar system. In order to assess the level of disruption, one also needs the rate of close encounters in young stellar clusters. These rates have already been calculated for a wide range of cluster properties (Adams et al. 2006; Proszkow & Adams 2009) and are used herein. The paper concludes, in Section 6, with a summary of our results and a discussion of their implications.

2. Formulation of the Problem

One useful way to specify the effects that passing stars can have on planetary systems is to define cross sections of interaction. For example, the scattering interactions could eject a

planet, increase the eccentricity, change the semimajor axis, and/or perturb the inclination angle of the orbit. For a given type of disruption, a solar system presents an effective target area for being disrupted by passing stars. With this definition, the effective interaction rate Γ for disruption is then given by the usual formula

$$\Gamma = n_*\langle\sigma\rangle\langle v\rangle \,, \tag{1}$$

where n_* is the mean density of stars in the environment, $\langle v\rangle$ is the mean relative velocity between systems, and $\langle\sigma\rangle$ is the cross section for the given mode of disruption. We note that the background environment determines the stellar density n_* and the distribution of relative velocities. As outlined below, the relative velocities follow a Maxwellian distribution characterized by the expectation value $\langle v\rangle$. The interaction cross section depends on this velocity distribution, so that we actually calculate the quantity $\langle\sigma\rangle_v \equiv \langle\sigma v\rangle/\langle v\rangle$, where the subscript denotes that the cross section depends on the velocity expectation values $\langle v\rangle$. For ease of notation, however, we drop the subscript for the remainder of the paper. In young embedded clusters, we expect $n_* \sim 100$ pc^{-3} and $\langle v\rangle \sim 1-2$ km/s; in the field (in the solar neighborhood) these quantities have typical values $n_* \sim 1$ pc^{-3} and $\langle v\rangle \sim 30-40$ km/s. Because of the velocity dependence of the cross sections, solar systems in the field (with high fly-by speeds) are, on average, less affected by passing stars.

To calculate the cross sections for interactions, we adopt the following approach. First we must specify the configuration of the solar system that will be targetted for disruption (for example, we can use the current set of four giant planets in our solar system, with their current masses and semimajor axes, all in orbit about a solar mass star). Next we must specify the background environment, which determines the distribution of relative velocities. For most of this work, we focus on the case where the target solar system encounters binaries. We then perform a large ensemble of numerical simulations, where the input parameters are specified according to a Monte Carlo scheme. The results are then used to calculate the probability of various outcomes and the corresponding cross sections (for further detail, see Laughlin & Adams 2000; Adams & Laughlin 2001; Adams et al. 2006).

In principle, the Monte Carlo sampling scheme should sample all possible encounters between binaries and the target solar system, including those with large impact parameters. In practice, however, only sufficiently close encounters have a non-negligible chance of affecting the planetary orbits. In order to conserve computer time, we thus make the following limitation. We treat the semimajor axes a of the binaries on a different footing than the others: The values of a are sampled uniformly out to $a_{\mathrm{max}} = 1000$ AU (more than 30 times the size of Neptune's orbit in our solar system). For a given value of a, and we then limit the possible range of impact parameters to fall within an area given by $A_0 = B\pi a^2$. With this sampling scheme, the cross section of interaction, for a given type of distruption event,

is given by

$$\langle\sigma\rangle = \int_0^{a_{\max}} p(a)da\, f_D(a)\left(B\pi a^2\right),\tag{2}$$

where $p(a)$ is the probability distribution for binaries having a semimajor axis a. The factor $f_D(a)$ represents the fraction of all encounters (within the pre-determined area $A_0 = B\pi a^2$) that results in the outcome of interest.

The formulation of equation (2) can be understood as follows: Consider a given outcome of interest, say, the ejection of Neptune. We only consider fly-bys that take place within the area $A_0 = B\pi a^2$, where a is sampled uniformly. If every encounter within this area leads to the ejection of Neptune, and all encounters outside this area (which are not computed) have no effect, then $f_D = 1$; the probability factor $p(a)$ corrects for the actual distribution of binary semimajor axis, and one can see that equation (2) provides the correct effective cross section. In practice, of course, only a small fraction of encounters lead to the ejection of Neptune so that $f_D \ll 1$. As long as we choose the factor B large enough, we are ignoring only distant encounters that have little contribution to the cross section. Nonetheless, since B is finite, this procedure leads to a lower limit on the cross section. We have run convergence tests with ever-increasing values of B and find that $B = 100$ is large enough to include essentially all relevant encounters. In most of this work we thus use $B = 100$, which provides a good compromise between computational speed and accuracy. For comparison, our previous work (Laughlin & Adams 2000; Adams & Laughlin 2001) used the smaller value $B = 4$, so that the reported cross sections (again presented as lower limits) were smaller than those obtained here by a factor of ~ 2.

The distribution $p(a)$ is determined by the observed binary period distribution, which is nearly uniform in the quantity $\log a$, but has a broad peak centered at period $P = 10^5$ days, which implies $a \approx 42$ AU for solar type stars (Duquennoy & Mayor 1991).

Within the scheme outlined above, encounters between a given solar system and a passing binary are specified by a large number of input parameters: We must specify the properties of the binary, including its semimajor axis a, orbital eccentricity e_b, the masses of the two stars M_{1*} and M_{2*}, and finally the phase of the binary orbit θ_b at the start of the encounter. The orbital elements (a, e_b) are sampled from their observed distributions (Duquennoy & Mayor 1991). Similarly, the stellar masses are sampled from a log-normal form of the stellar initial mass function (consistent with that advocated by Adams & Fatuzzo 1996 and Chabrier 2003). The phase angle θ_b of the orbit is sampled uniformly over $[0, 2\pi]$. Next we must specify the incoming velocity v_∞ of the solar system with respect to the binary center of mass; this speed is sampled from a Maxwellian distribution with a velocity dispersion v_b that characterizes the background environment (e.g., a cluster). The remaining variables are the three angles (θ, ψ, ϕ) necessary to specify the direction and orientation of the

encounter, and finally the impact parameter ϖ. The impact parameter is chosen randomly within a circle of radius $10a$ centered on the binary center of mass (corresponding to the choice $B = 100$ in equation [2]).

Using a Monte Carlo scheme to select the input parameters according to the distributions described above, we carry out a large ensemble of scattering simulations. For most cases we find that the number of simulations $\mathcal{N}_E = 80,000$ is large enough to provide good statistics. The outcomes of these numerical experiments are then used to compute the fraction f_D of disruptive encounters for a given type of outcome. The resulting errors due to incomplete sampling are typically 5 percent or less, but can be larger for rare events (e.g,. for planet ejections, the sampling errors are ~ 10 percent).

Each simulation is thus an N-body problem. For most cases, $N = 7$, where the target system consists of four giant planets orbiting a host star and interacts with a binary. The equations of motion are integrated using a Bulirsch-Stoer method (Press et al. 1986), which allows for rapid integrations and high accuracy. Because we are interested in the planetary orbits, which only contain a small fraction of the total energy of the N-body system, the simulations must conserve the total energy to high accuracy in order to determine the final orbital elements. For example, the energy contained in the orbit of Neptune, the least bound planet, is typically 10^4 times smaller than the binding energy of a binary, or the initial gravitational potential energy between the binary and the solar system. In practice, our individual simulations have an accumulated error of only one part in 10^8, so that orbital changes are safely resolved.

3. Results for the Cross Sections

Using the formulation described in the previous section, we have performed several large ensembles of numerical scattering simulations. Unless stated otherwise, we consider the solar systems to have four giant planets and to interact with passing binary stars. We then consider a number of different solar system architectures for the starting states, as outlined below. To obtain reasonable statistics within the Monte Carlo scheme, the number of individual numerical experiments for each solar system architecture must typically be of order $\mathcal{N}_E \approx 80,000$. This choice produces relative errors (due to incomplete sampling) of order 5 percent or smaller.

In the first set of simulations, we consider the target system to be an analog of our present-day solar system. In this case, we place the four giant planets in orbit about a solar mass star and give the planets their current masses and semimajor axes. The eccentricities

are all set to zero, however, so that we can measure the eccentricity increases produced by the scattering encounters. From the results of these experiments, we compute the cross sections for orbital disruption of each of the four planets (as outlined in the previous section). The results are shown as the solid blue curves in Figure 1, which also presents the cross sections for a more compact starting configuration (described below). The error bars (not shown) due to incomplete Monte Carlo sampling correspond to relative errors with a root-mean-square (RMS) value of $\sim$4.4%.

In Figure 1, and throughout this paper, the cross sections for increasing the eccentricity to $e = 1$ incorporate all of the ways that the planet can be removed from its solar system. These channels include [1] actually increasing the eccentricity to $e \geq 1$, which includes both hyperbolic orbits and planetary orbits that intersect the host star, [2] ejection from the solar system by increasing the kinetic energy so that the orbit is unbound, and [3] capture by one of the (two) passing stars. These channels are not mutually exclusive, but the simulations are stopped after one of these events takes place. However, these channels only include ejection processes that happen during or immediately after the encounter (we denote these processes as prompt ejections). In other cases, the planets are scattered into high eccentricity orbits, so that the orbits cross each other. With these configurations, in the absence of resonance, the planets will eventually experience close encounters, which in turn lead to ejections or collisions (we denote this process as delayed ejection). The cross sections for delayed ejections will be considered later.

For comparison, we also present the results from a series of numerical experiments using a more compact orbital architecture (shown as the red dashed curves in Figure 1), which is motivated by the Nice model of solar system formation (Gomes et al. 2005). Although the Nice model has a number of variations, one feature is that the giant planets could have formed with a more compact configuration than that of the present day. For this case, we fix the orbit of Jupiter at $a_J = 5.2$ AU, and then let each successive planet have a semimajor axis that is larger than the previous one by a factor of 5/3. This evenly-spaced solar system thus extends out to only 24 AU. The results, shown in Figure 1, indicate that the cross sections for the compact configuration are somewhat smaller than those obtained with the current semimajor axes. For this compact solar system, the RMS errors (not shown) due to incomplete sampling are $\sim$4.6%.

Next we consider an even more compact orbital configuration, again motivated by the Nice model, where the four giant planets are in mutual mean motion resonance (MMR). In this case, we choose the starting semimajor axes to have values of $a = 5.88$ AU (Jupiter), 7.89 AU (Saturn), 10.38 AU (Uranus), and 12.01 AU (Neptune). With these semimajor axes, Jupiter and Saturn are in a 3:2 MMR, Saturn and Uranus are in a 3:2 MMR, while
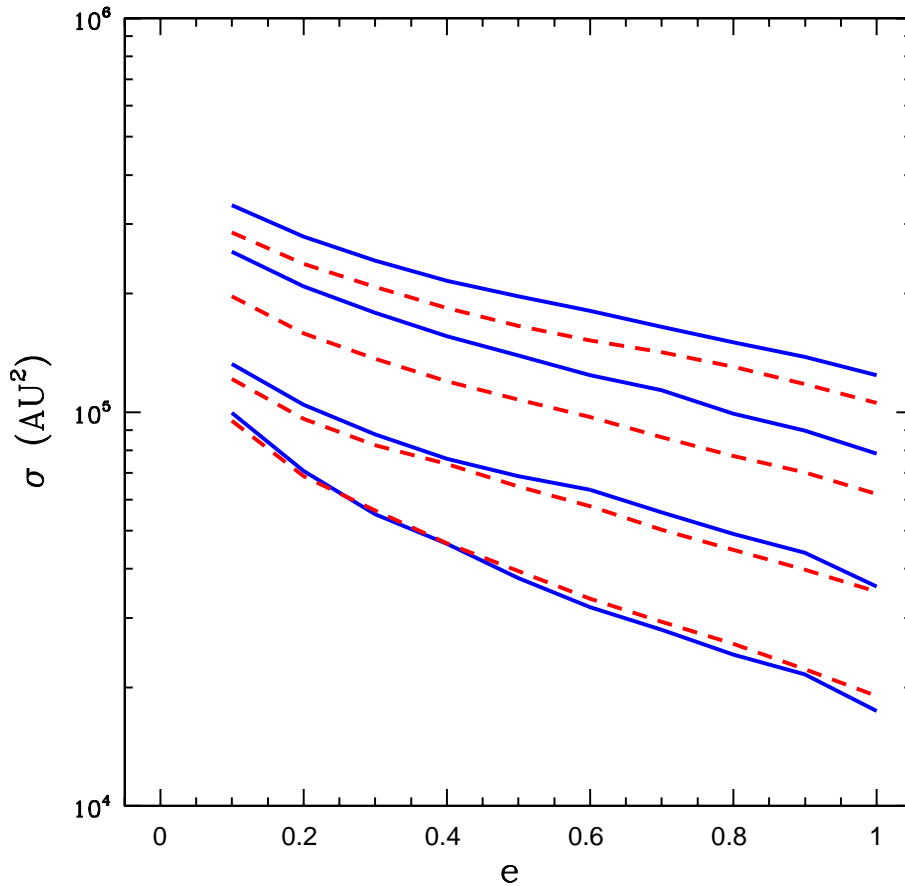
Fig. 1.— Cross sections for current solar system architecture and for a more compact configuration movitated by the Nice model. For the current solar system (solid blue curves), the four giant planets are started with their current semimajor axes and zero eccentricitiy. For the compact configuration (dashed red curves), the planets are started with semimajor axes having a fixed ratio $a_{j+1}/a_j = 5/3$, where Jupiter ($j = 1$) is started at its present location $a_J = 5.2$ AU. For both sets of cross sections, the curves, from top to bottom, correspond to Jupiter (bottom), Saturn, Uranus, and Neptune (top).
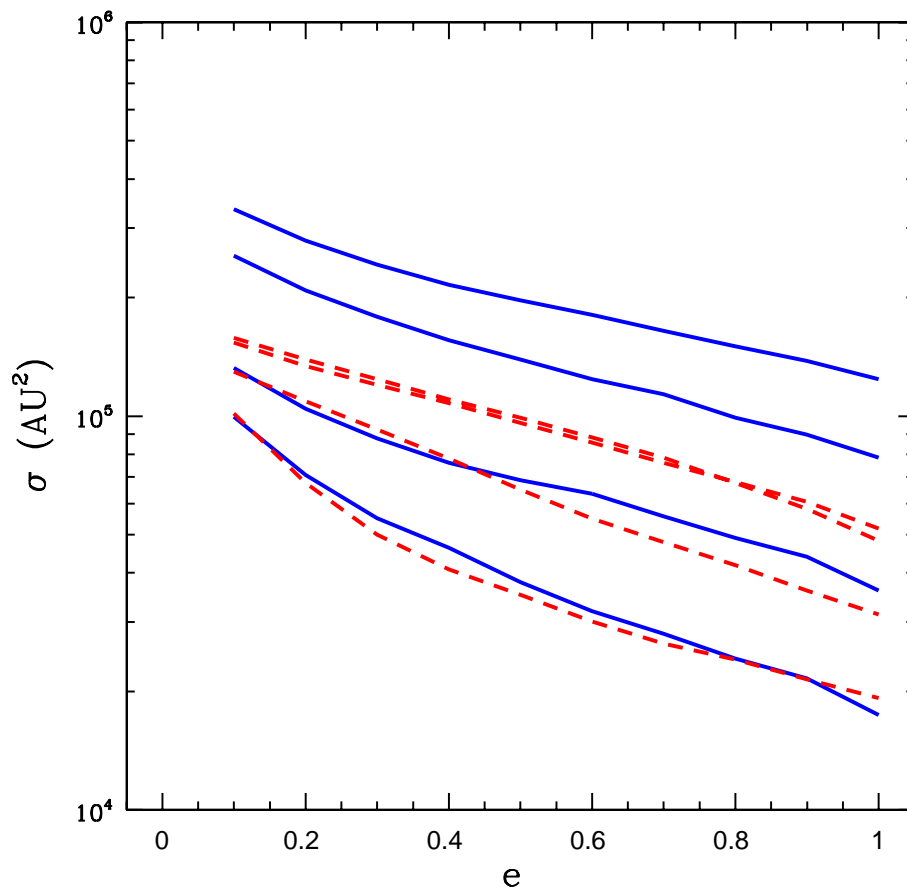
Fig. 2.— Cross sections for current solar system architecture and for a resonant configuration movitated by the Nice model. For the current solar system (solid blue curves), the four giant planets are started with their current semimajor axes and zero eccentricitiy. For the resonant configuration (dashed red curves), the planets are started with semimajor axes a = 5.88, 7.89, 10.38, and 12.01 AU (for the analogs of Jupiter to Neptune). For both sets of cross sections, the curves, from top to bottom, correspond to Jupiter (bottom), Saturn, Uranus, and Neptune (top).

Uranus and Neptune are in a 5:4 MMR (for further discussion of this initial state, and others, see Batygin & Brown 2010; Nesvorný & Morbidelli 2012; Li & Batygin 2014). Note that the semimajor axis ratios do not imply period ratios with exact integer values (although they are close). All of the orbital elements must be chosen properly to put the system in mutual MMR, and this requirement displaces the period ratios somewhat. Nonetheless, the resonance angles of the system (for all three planet pairs) are librating in the initial state, as required for MMR. With this initial state, the solar system is much more compact than at the present epoch, and the cross sections for interactions are smaller. This trend is illustrated in Figure 2, which compares the cross sections with those obtained for solar systems with the standard starting configuration. To leading order, the smaller cross sections obtained for the resonant architecture are a direct consequence of the smaller geometrical size. However, closer inspection of the results suggests that the cross sections are larger than the smaller size would imply (see the analysis of the following section). For example, the cross sections for changing the eccentricity of Uranus and Neptune are comparable. In this compact state, planet-planet interactions can be important and act to increase the the cross sections of Uranus (and Saturn) beyond the values obtained for more widely separated orbits.

In addition to changes in the orbital elements of the individual planets, as shown in Figure 2, scattering interactions can remove solar systems from their resonant states. The energy required to remove a planetary system from resonance is much less than that required to eject a planet, or even to substantially change its orbital elements. To address this issue, we have run an additional series of numerical simulations to determine the fraction of systems that are removed from their initial resonant state due to passing binaries. As before, the ensemble size $\mathcal{N}_E \approx 80,000$, although the simulations take longer because the resonance angles must be monitored for several libration times after the encounters. The result of this set of experiments is the cross section for removing the solar system from its initial resonant state, namely

$$\langle \sigma \rangle_{\rm res} \approx (2,280,000 \pm 20,800)\,{\rm AU}^2\,. \tag{3}$$

This cross section is about 20 times larger than that required to eject Neptune from the solar system in its normal state, and nearly 40 times larger than the cross section to eject Neptune from the compact, multi-resonant state. If the removal of the system from resonance results in orbital instability over longer time intervals, then the multi-resonant state could be more sensitive to disruption from passing stars than the standard solar system architecture. We have carried out 70 longer-term integrations for post-encounter systems and find that all but one are stable on time scales of ~ 1 Myr. Other authors (Batygin & Brown 2010; Nesvorný & Morbidelli 2012) also find that multi-resonant states can be unstable due to perturbations (generally due to a planetesimal disk), and can eject planets, but more follow-up integrations are required to assess the probability of significant instability.
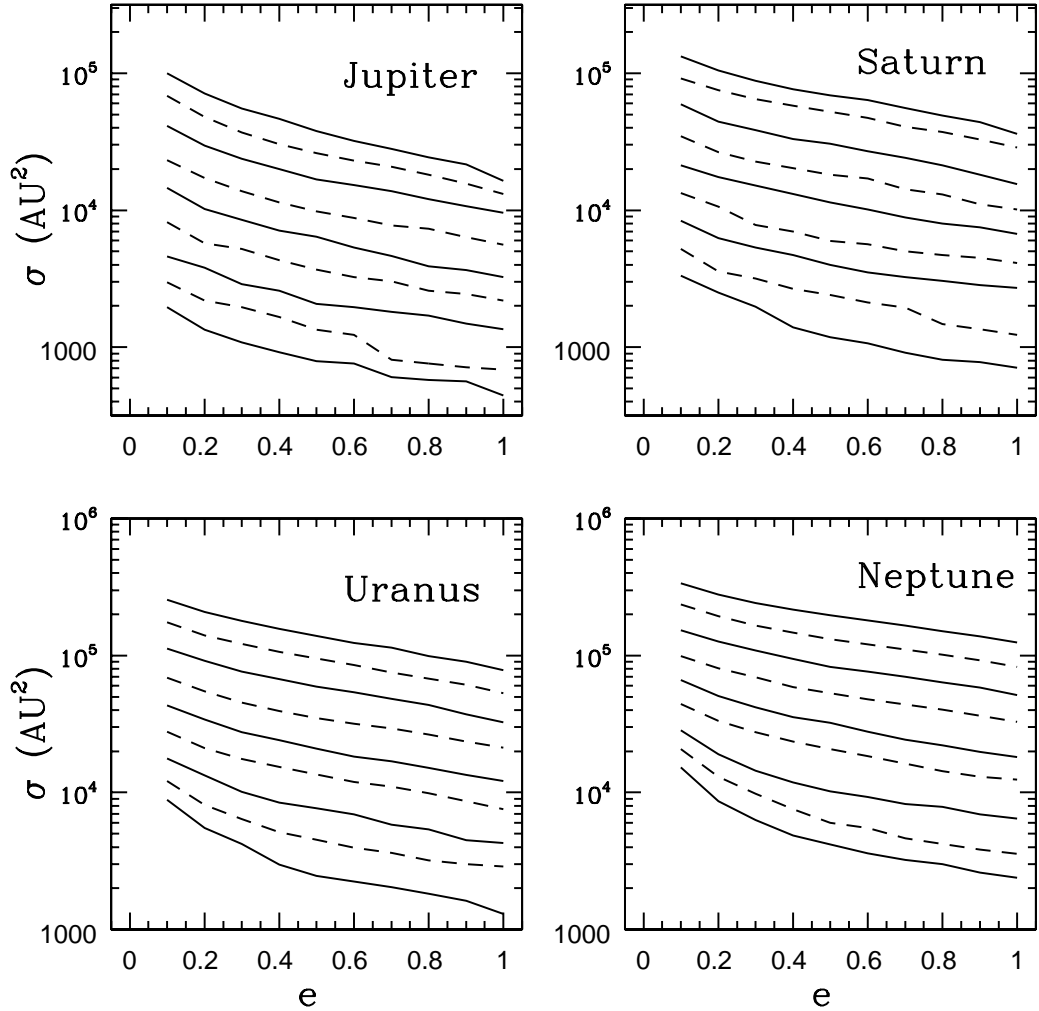
Fig. 3.— Cross sections for current solar system architecture for a wide range of velocity dispersions for the background cluster. For four giant planets of the solar system are started with their current semimajor axes and zero eccentricitiy. Each panel shows the cross sections to increase orbital eccentricity for Jupiter (upper left), Saturn (upper right), Uranus (lower left), and Neptune (lower right). The velocity dispersions fall in the range from 1 km/s (uppermost curves in each panel) to 16 km/s (lower curves), and are equally spaced logarithmically (by factors of $\sqrt{2}$).

The results reported thus far have all been calculated for cases where the velocity dispersion $v_b = 1$ km/s, a typical value for an embedded cluster environment (Lada & Lada 2003; Porras et al. 2003). Next we consider the dependence of the cross section on the velocity dispersion of the background environment. As is well known, interaction cross sections for high speed encounters, such as in the field (Laughlin & Adams 2000), are much lower than those in clusters (Adams et al. 2006), and the velocity dependence is relatively steep (Adams & Spergel 2005; Dukes & Krumholz 2012). To study this dependence, we consider ensembles of numerical simulations with different values of velocity dispersion v_b. More specifically, we consider solar system starting with the current value of semimajor axes, and v_b in the range from 1 km/s to 32 km/s, varied by factors of $\sqrt{2}$ (so they are evenly spaced in a logarithmic sense). For the low end of this range of v_b, we can use the usual number $\mathcal{N}_E = 80,000$ of trials in the ensemble for each value of v_b. For the larger values of v_b, however, the cross sections are lower, and disruptive events are rare, so that we need larger values of $\mathcal{N}_E$ to obtain good statistics (we find that the choice $\mathcal{N}_E \approx 200,000$ is usually large enough).

The interaction cross sections produced by this study are shown in Figure 3, where each panel corresponds to the results for one of the giant planets. The cross sections are plotted as a function of the post-encounter eccentricity e, for each choice of velocity dispersion v_b. Figure 3 shows that the cross sections are almost evenly spaced in a logarithmic sense, with the lowest (highest) velocity dispersions producing the largest (smallest) largest cross sections. This finding suggests that the cross sections — to leading order — display a power-law dependence on the velocity dispersion. This claim is verified in the following section.

Next we consider the effect of changing the mass M_* of the host star. Figure 4 shows the cross sections for systems with the current solar system architecture and varying stellar masses, from $M_* = 0.25 - 2.0 M_\odot$. For these numerical experiments, the solar systems are all started with four planets that have the same masses and semimajor axes of the giant planets of our solar system. These analogs are labeled as 'Jupiter' through 'Neptune', although the host star can have a mass that differs from the Sun. As expected, the cross sections shown in Figure 4 decrease as the stellar masses increases. Unlike the case of varying the velocity dispersion, however, the cross sections, considered as a function of eccentricity increase, do not display as much self-similarity: The cross sections decrease more steeply with eccentricity as the mass of the host star increases. Nonetheless, for a given value of eccentricity increase, cross sections for the four planets (with their four values of a) all show the nearly same (power-law) scaling with stellar mass.

Notice that changing the stellar mass is (in one sense) akin to changing the planetary masses, because the mass ratios are the most important variables. However, this association is not an equivalence: The masses of the passing binaries also enter into the problem,
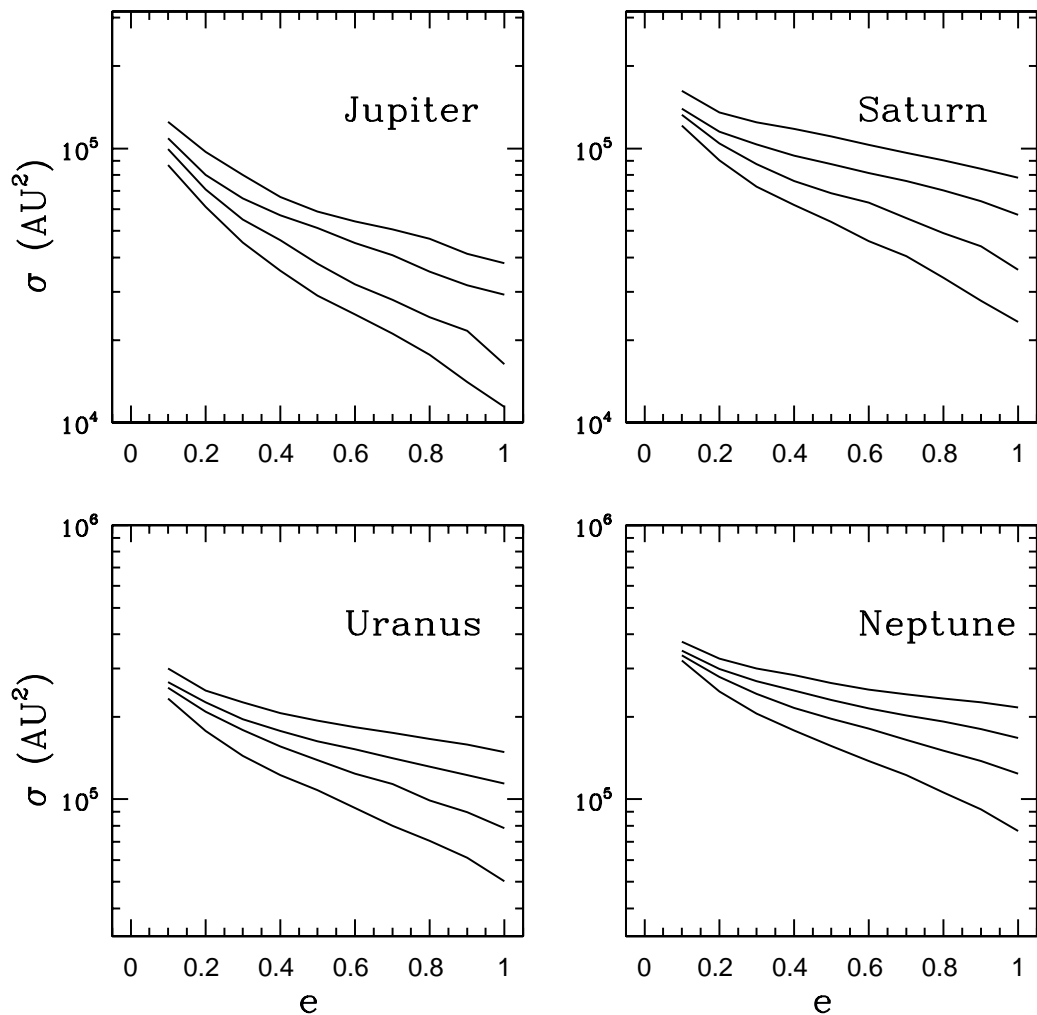
Fig. 4.— Cross sections for a range of masses of the host star. Each case uses analogs of the four giant planets of our solar system, where the planets start with the current semimajor axes and zero eccentricitiy. Each panel shows the cross sections to increase orbital eccentricity for the analog Jupiter (upper left), Saturn (upper right), Uranus (lower left), and Neptune (lower right). The four curves in each panel correspond to four stellar masses, $M_* = 0.25$, 0.5, 1.0, and 2.0 $M_\odot$, from top to bottom.

and their mass distribution is kept invariant. In addition, if the masses of the planets are increased to the point where the planet-planet interactions play a role, then self-excitation of eccentricity can produce larger cross sections. This issue is addressed below where we consider solar systems with larger planets. We expect interactions to be important in the regime where the angular momentum exchange time scale between planets is comparable to the encounter timescale. The exchange time scale can be determined, but the calculation is different for widely separated planets where the secular approximation is valid and for the resonant case (for further discussion, see Batygin & Morbidelli 2013).

For the starting configurations used thus far, the initial orbital eccentricities of the planets have been taken to be zero. Given this choice, the resulting cross sections represent the cross sections for increasing eccentricity (which cannot decrease from its initial value). However, for the related problem of single stars interacting with binaries, an important difference arises between starting states where the binary has zero eccentricity and states where the binary has small but finite eccentricity (Heggie & Rasio 1996). One might worry that the cross sections calculated herein could be affected by introducing small starting eccentricities for the planetary orbits. We have explored this possibility by using two additional starting configurations for the solar system. In one case, the planetary orbits are started with their currently observed eccentricities, $e = 0.049$, 0.057, 0.045, and 0.011 for Jupiter, Saturn, Uranus, and Neptune, respectively. In the second case, the planetary orbits are all started with a larger value of eccentricity $e = 0.10$. The resulting cross sections are shown in Figure 5, along with our previous results with zero starting eccentricity. As shown in the Figure, all of the cross sections converge to the same values as long as the final eccentricity is moderately larger than the starting values. The difference between results obtained starting with zero eccentricity and those where the orbits have their current eccentricity is modest. For the larger starting values $e = 0.10$, the cross sections for reaching $e = 0.10$ are enormous of course, much larger than the limits of the plot (and hence are not shown). Even for this starting state, however, the cross sections have almost converged to their "natural" values for $e \gtrsim 0.20$, except for the case of Uranus; for this planet, the cross sections for eccentricity excitation only converge for $e \gtrsim 0.35$.

The results illustrated in Figure 5 indicate that the problem of solar systems interacting with passing binaries is somewhat different than that of single stars interacting with binaries (Heggie & Rasio 1996). Starting with zero eccentricities has a larger effect in the binary-single-star setting. One difference between the two cases is that of symmetry: For a single star passing by a binary with zero eccentricity, the incoming trajectory is the same as the outgoing trajectory provided that the encounter is distant (so that the binary orbit can be considered as a ring of mass); this symmetry cancels some of the forcing. However, this symmetry is absent for solar system scattering, even when the planetary orbits are circular.
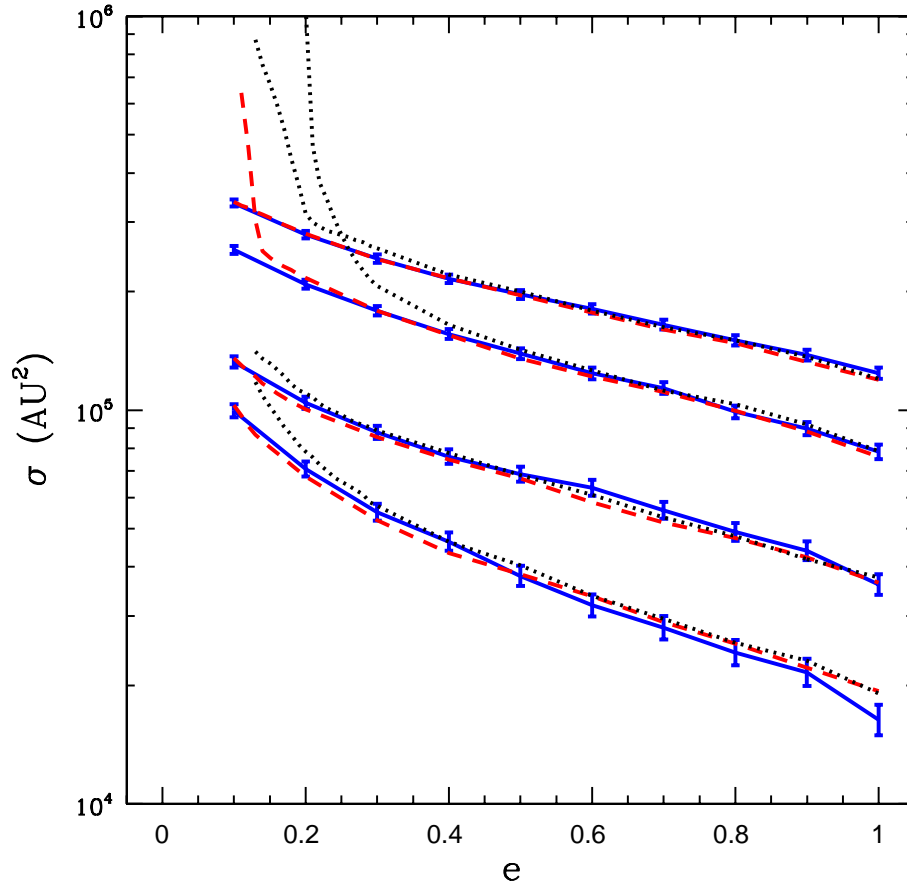
Fig. 5.— Cross sections for the solar system planets and varying initial eccentricities of the planetary orbits. For all cases, the four giant planets of our solar system are started with their current semimajor axes. The solid blue curves show the results for zero initial eccentricitiy; the dashed red curves show the results where the planets start with their current orbital eccentricities ($e = 0.049$, 0.057, 0.045, and 0.011); the black dotted curves show the results where the starting orbits all have $e = 0.10$. Cross sections are given for Jupiter (bottom curves), Saturn, Uranus, and Neptune (top curves).

The binaries that impinge upon the solar systems are themselves eccentric, where e is drawn from the observed binary eccentricity distribution (which favors high e). In addition, the solar systems have four planets, with different orbital phases, and this property also breaks the symmetry (albeit to a lesser degree). Another difference between the two scattering problems is that the cross sections of this paper are averaged over an ensemble of different binary properties and different encounter parameters. The binary scattering results (Heggie & Rasio 1996) show that the the difference between finite eccentricity and circular orbits is largest for distant encounters, but the effect (the change in eccentricity) is largest for close encounters (see their Figure 2). The cross sections of this paper include both regimes, but the cross section is dominated by the close encounters where the results for $e = 0$ and $e \neq 0$ are similar. As a result, starting the planetary orbits with non-zero eccentricity has only a modest effect on the cross sections considered in this paper (provided that one considers post-encounter eccentricities sufficiently larger than the starting values).

Next we consider the effects of planetary mass on the scattering cross sections. The results are shown in Figure 6 for the usual Solar System parameters and for an analog solar system where all of the giant planets have the mass of Jupiter ($m_P = 1m_J$). Both classes of systems start with the same semimajor axes (the present-day values in our system) and zero eccentricity. The figure shows that the cross sections for increasing the eccentricities of Neptune and Uranus are largely unaffected by the increase in planetary mass, but the cross sections for Jupiter and Saturn are somewhat larger. Note that the cross sections are plotted only for eccentricity values $e \geq 0.20$. Within such a massive planetary system, small eccentricities ($e \sim 0.10$) are easily excited by planet-planet interactions; as a result, the cross sections for eccentricity increase — as determined through our numerical scheme — are extremely large and are not plotted in the figure.

The numerical results for the cross sections can be understood as follows: To leading order, we often expect the planets to act as test particles, so that the cross sections should not be sensitive to the planetary masses. For sufficiently massive planets, however, an increase in the eccentricity of one planet can lead to significant perturbations acting on the other planets, thereby leading to increased eccentricity excitation. By increasing the mass of all of the planets to that of Jupiter, the resulting solar systems are more excitable. The largest increase in the cross sections, which occurs for Jupiter and for low eccentricties, is only a factor of ~ 2; most cross sections experience smaller changes. These results are generally consistent with the idea that our Solar System is "full", i.e., no additional planets and little additional mass can be added to the extant planets without rendering the system unstable. In fact, even the current solar system is unstable on sufficiently long time scales (Batygin & Laughlin 2008; Laskar & Gastineau 2009).
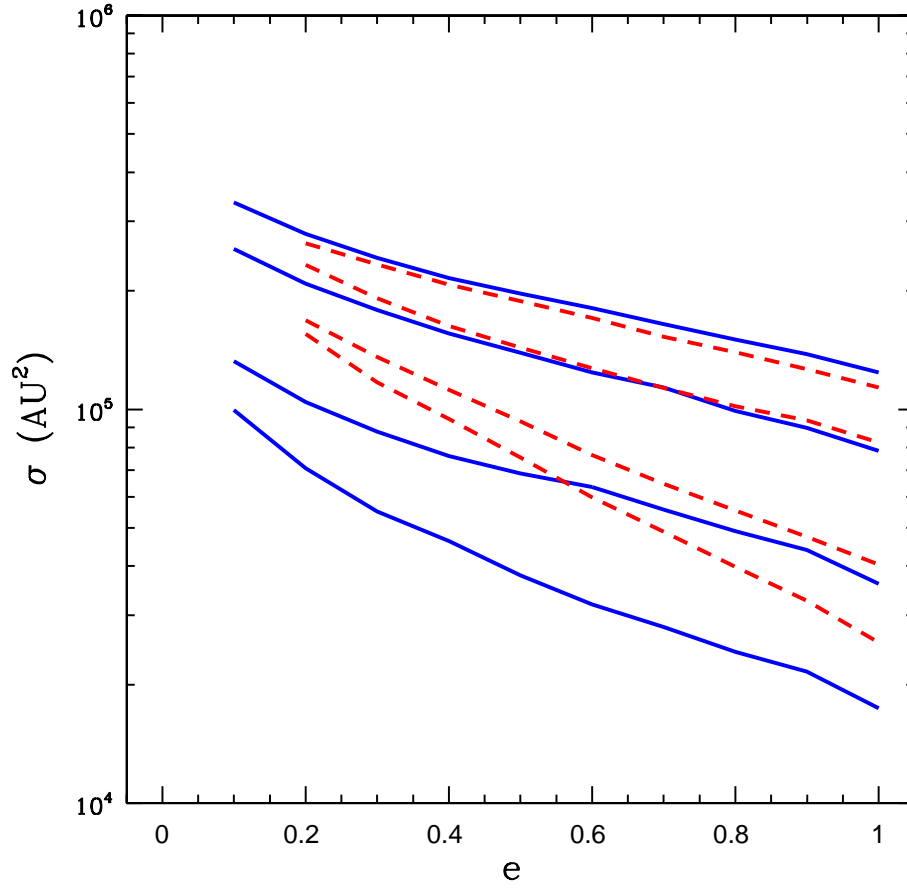
Fig. 6.— Cross sections for the current solar system architecture (solid blue curves) compared with cross sections for systems where the giant planets all have mass $m_P = 1m_J$ (dashed red curves). In both cases, the planets are started with the current semimajor axes of the giant planets in our Solar System and with zero eccentricity. Cross sections are shown for analogs of Jupiter (bottom curves), Saturn, Uranus, and Neptune (top curves).
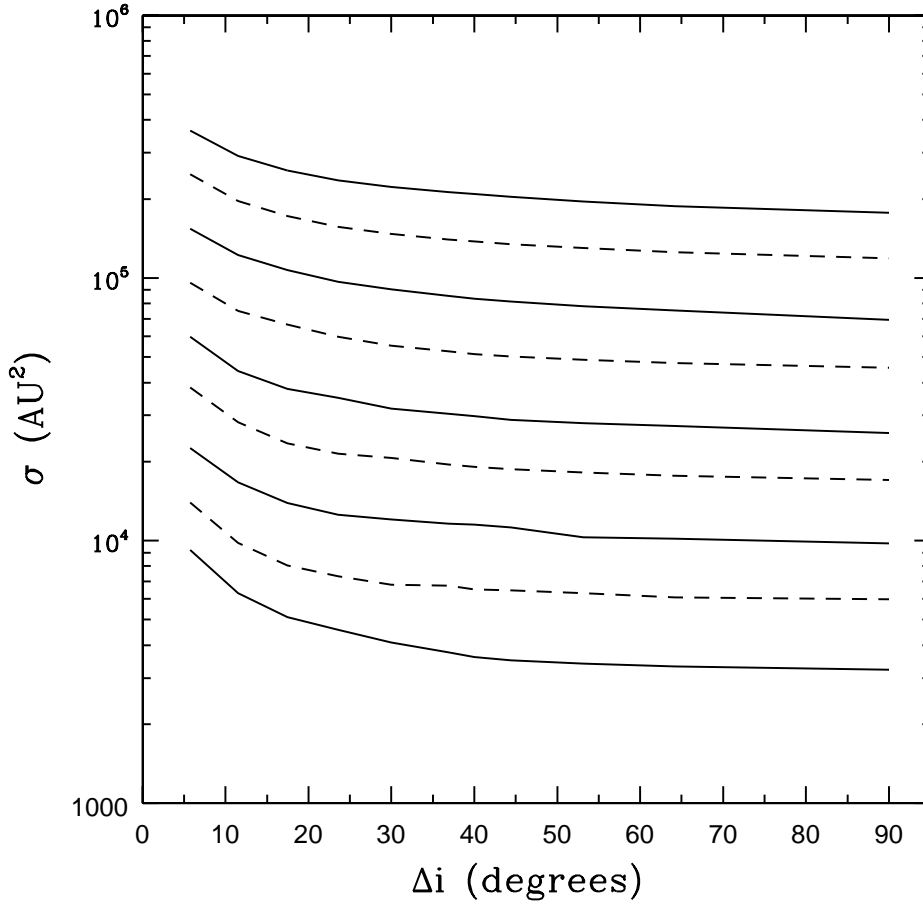
Fig. 7.— Cross sections for increasing the spread of inclination angles of the planetary orbits. All of the giant planets are started in the same plane; the quantity Δi is the total range of inclination angles of the four orbits after the encounters. Cross sections are shown for a variety of velocity dispersions, from $v_b = 1$ km/s (top curve) to $v_b = 16$ km/s (bottom curve), where the values are evenly spaced logarithmically (by factors of $\sqrt{2}$).

Another way in which planetary orbits can be altered by scattering encounters is by changing their inclination angles. For all of the simulations, we start the four giant planets in the same plane (so that $i_J = i_S = i_U = i_N = 0$). After the encounters, the inclination angles of the four planets are, in general, nonzero. We define the post-encounter spread Δi of the inclination angles according to the expression

$$\Delta i \equiv \max \left\{ \cos^{-1} \left[\frac{\mathbf{J}_j \cdot \mathbf{J}_k}{J_j J_k} \right] \right\} , \tag{4}$$

where the $\mathbf{J}_i$ are the angular momentum vectors of the planetary orbits and where the indices run through all four of the giant planets. The resulting cross sections for increasing the spread of inclination angles is shown in Figure 7. The Figure shows the cross sections for a range of velocity dispersions of the background cluster, from $v_{\rm b} = 1$ km/s to $v_{\rm b} = 16$ km/s, where the values are spaced by factors of $\sqrt{2}$. The cross sections are almost evenly spaced in the semi-logarithmic plot and have nearly the same shape as a function of Δi. These properties indicate that the cross section has a power-law dependence on $v_{\rm b}$ (see Section 4).

In general, increases in the inclination angles are positively correlated with increases in eccentricity. This result is not unexpected, as changes in both orbital elements correspond to disruption of the initial states. To illustrate this trend, we plot the increases in the spread of inclination angle Δi versus the post-encounter eccentricity in Figure 8. The two variables are in fact well correlated, but the range of possible Δi values for a given eccentricity e is large. As a result, in the figure we plot the mean values of Δi averaged over a bin of width $\Delta e = 0.05$. With this choice of binning, the data show a well-defined correlation, where the spread in the inclination angles grows to about 80° as the eccentricity grows to unity. The four curves shown in Figure 8 correspond to the four giant planets. Note that the orbits of all four planets show the same general trend.

The cross sections discussed thus far correspond to the immediate, post-encounter properties of the solar systems. In addition to immediate ejection, however, the solar systems can be rendered sufficiently unstable so that they eject planets long after the scattering encounters are over. These longer term ejection events can be divided into (at least) two types. In the first — and most unstable — case, the scattering encounters leave the planetary orbits with high enough eccentricity so that adjacent orbits cross. Most orbiting-crossing systems will eventually eject one of their planets, provided that the system is not in a mean motion resonance; furthermore, perturbations due to stellar encounters are unlikely to place a planetary system in resonance. We address the effects of this type of instability by finding the cross sections for producing orbit-crossing planetary systems (see below). In the second case, systems with more modest eccentricities can be unstable over long spans of time. In order to assess the effects of this latter class of outcomes, the post-encounter systems must
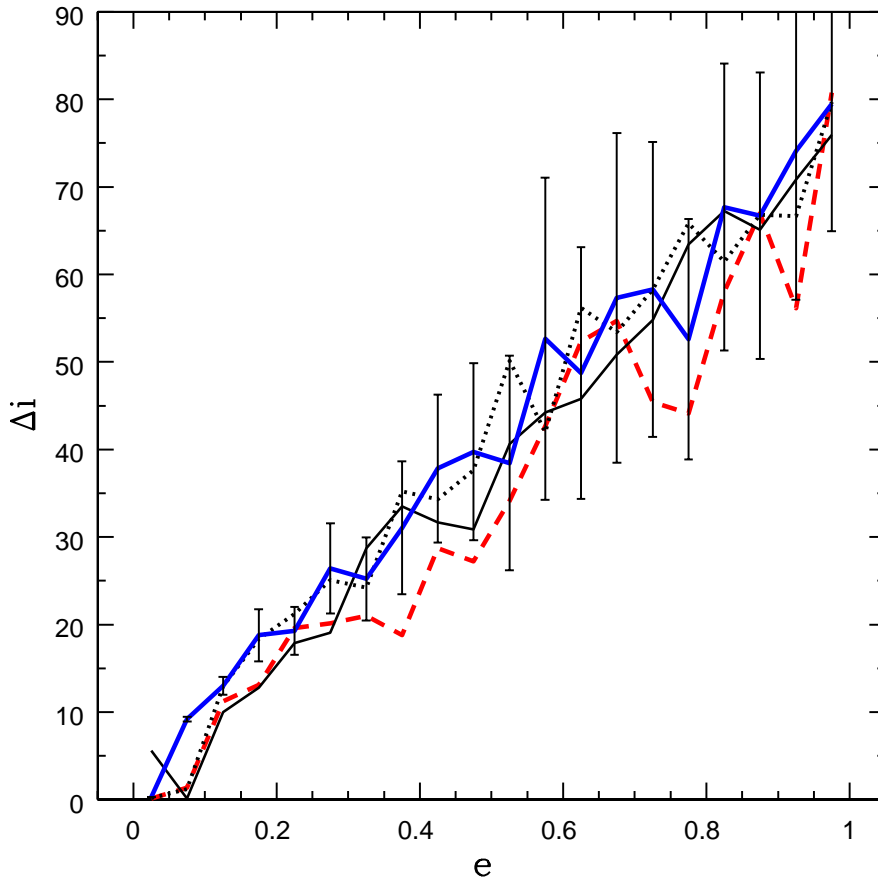
Fig. 8.— Correlation between eccentricity increases and increases in the spread of inclination angles of the planetary orbits. All of the giant planets are started in the same plane with circular orbits; the quantity Δi is the total range of inclination angles of the four orbits after the encounters. Correlations are shown for the orbital elements changes of Jupiter (heavy dashed red curve), Saturn (black solid curve), Uranus (black dotted curve), and Neptune (heavy blue solid curve). For each planet, the inclination angle increases are binned over a range $\Delta e = 0.05$. Although the correlation is well-defined, the range of Δi for a given value of e is relatively large. The error bars (shown for the Neptune curve only) depict the standard deviations.
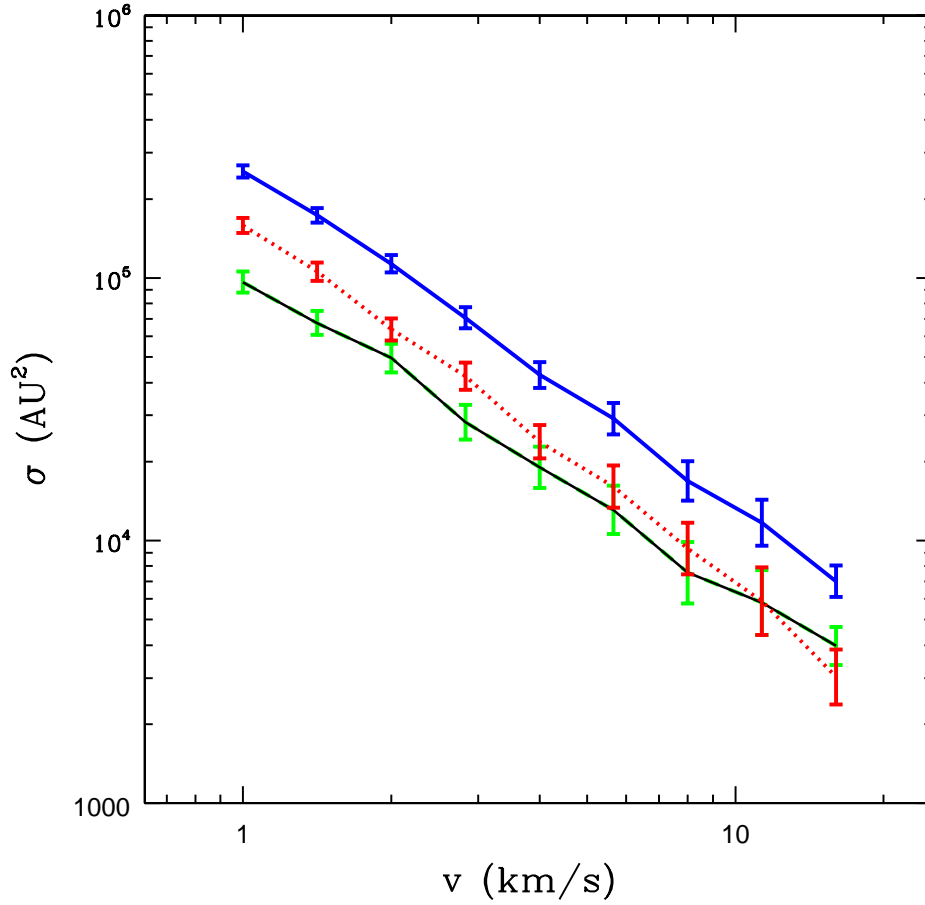
Fig. 9.— Cross sections for the ejection of at least one planet as a function of velocity dispersion v_b in the cluster. The target systems have four giant planets with the masses and semimajor axes of our solar system bodies. Cross sections are shown for three cases: increases in eccentricity large enough to produce orbit crossing (solid dark curve), direct ejection of a planet (dotted red curve), either channel of ejection (solid blue curve).

be integrated over typical stellar ages (billions of years). This task is beyond the scope of this present work, but provides an interesting problem for the future.

Using the results of our numerical experiments, we can calculate the cross sections for the scattering interactions to leave any two orbits with high enough eccentricities to cross. For the case of the analog solar system, where the four giant planets have their current masses and semimajor axes, the resulting cross sections are shown in Figure 9. Three sets of cross sections are shown as a function of the velocity dispersion v_b of the background cluster. The cross sections for the post-encounter system to have an orbit-crossing configuration are shown as the lower, green solid curve in the figure. For the calculation of this cross section, only systems where all of the planets are retained by the host star are included. The cross sections for the system to eject any planet (including those planets captured by the passing stars) are shown as the red dotted curve. Finally, the total cross sections for ejection, including both direct ejection of a planet and/or crossing orbits, are shown as the blue solid curve in the figure. The error bars depict the uncertainties in the cross sections due to incomplete Monte Carlo sampling. Note that the cross sections for orbit crossing and the cross sections for direct ejection are roughly comparable, with the latter slightly larger (except at high velocity dispersion, where they are the same within the sampling uncertainties). The total cross section for ejection is thus larger than that for direct ejection by a factor of ~ 2. This statement holds only for the current solar system architecture, but remains valid over the range of velocity dispersion shown here ($v_b = 1 - 16$ km/s).

We can now compare the results for the standard solar system architecture with that of the more compact configuration motivated by the Nice model. Here we consider only the most compact version where the planets are in multiple mean motion resonances (see Figure 2). The compact configuration is expected to have lower cross sections for direct ejection. But the orbits are closer together, so that less eccentricity excitation is required to produce crossing orbits. On the other hand, the semimajor axes are smaller, which lowers the cross sections for eccentricity increase. We find here that the cross sections for orbit crossing are comparable, $\langle\sigma\rangle = 96,500 \pm 3750$ AU^2 for the standard configuration versus $\langle\sigma\rangle = 92,200 \pm 3710$ AU^2 for the compact multi-resonant case. However, the cross section for direct ejection is larger for the standard solar system by a factor of 1.5, so that the total ejection cross section remains larger by a factor of ~ 1.25.

Although the semimajor axes of planetary orbits are altered less dramatically than the eccentricities and inclination angles during scattering encounters, the values of a are nonetheless affected. The possible variations are quantified in Figure 10, which shows the cross sections for producing relative changes $(\Delta a)/a$ in the semimajor axes of the four giant planets. This ensemble of numerical simulations uses the standard solar system architecture
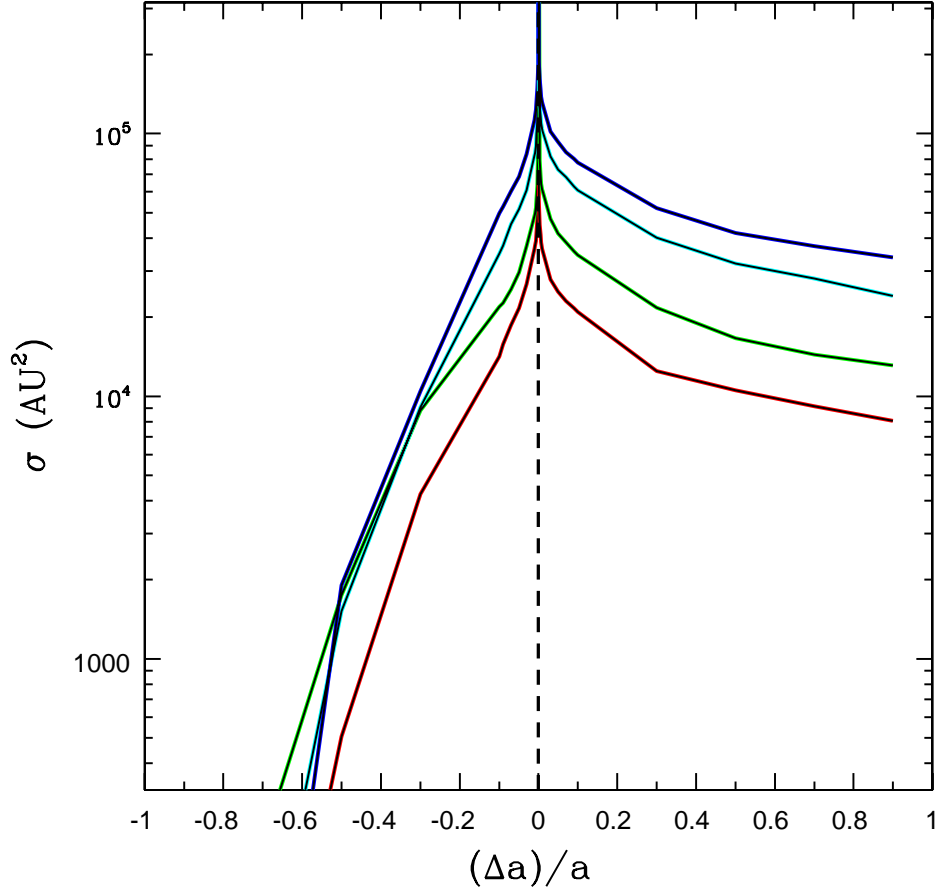
Fig. 10.— Cross sections for changes in the semimajor axis of the planetary orbits due to scattering encounters. The target systems are analogs of our Solar System, with the four giant planets initially in circular orbits with the current values of their semimajor axes. The plots shows the cross sections for relative changes $(\Delta a)/a$ in the semimajor axis for the orbits of Jupiter (lower red curve), Saturn (green curve), Uranus (cyan curve), and Neptune (upper blue curve).

as initial conditions, where the planets have their current masses and semimajor axes. The velocity dispersion of the background cluster is taken to be $v_b = 1$ km/s. As expected, the cross sections are largest for Neptune (top blue curve) and smallest for Jupiter (bottom red curve). As a crude approximation, the cross sections are proportional to the starting semimajor axes of the planets (although closer inspection shows the scaling is somewhat less steep than linear).

Scattering encounters can cause the semimajor axes to become either smaller or larger, corresponding to the loss or gain of orbital energy. However, Figure 10 shows that the process is highly asymmetric, where the orbits are much more likely to become larger (gain energy) than to move inward (lose energy). The scattering encounters rarely reduce the semimajor axes by more than a factor of two. Moreover, the magnitude of the cross sections are relatively small. More specifically, the cross sections for changing the initial semimajor axes by 10% are roughly comparable to — but somewhat smaller than — the cross sections for ejecting a planet (compare Figures 1 and 10). One might think that cross sections for moderate changes Δa would be larger than those for ejection. However, the cross sections for changes in semimajor axis do not include the ejections themselves, i.e., they are the cross sections for changing the semimajor axis with the planet remaining bound to its host star. For large changes in a, there is not much parameter space where a is increased but the planet remains bound (thereby leading to the values shown in Figure 10). Notice also that the figure does not show cross sections for overly small values of $(\Delta a)/a$; the cross sections become singular in the limit $(\Delta a)/a \to 0$, as marked by the vertical dashed line.

The cross sections considered thus far correspond to interactions between solar systems and passing binaries. On the other hand, roughly half of the stellar population consists of single stars, so that the corresponding cross sections for singles must also be determined. Since we are primarily interested in a comparison between the cross sections for single stars and binaries, it is crucial to use the same sampling for all of the parameters in the problem. Toward this end, we use exactly the same procedure as before (outlined in Section 2), but let the mass of the second star go to zero. In this limit, the other, single star automatically resides at the center of mass of the system (and the value of the binary eccentricity becomes irrelevant). The resulting cross sections for single stars interacting with solar system analogs are shown in Figure 11. As before, the initial solar systems consist of four giant planets with the masses and semimajor axes of the present day Solar System (but with zero starting eccentricity). Each panel shows the interaction cross sections for eccentricity increases for a given planet (as labeled). Results are shown for four values of the velocity dispersion of the background cluster, i.e., $v_b = 1, 2, 4,$ and 8 km/s (ordered from top to bottom in each panel).
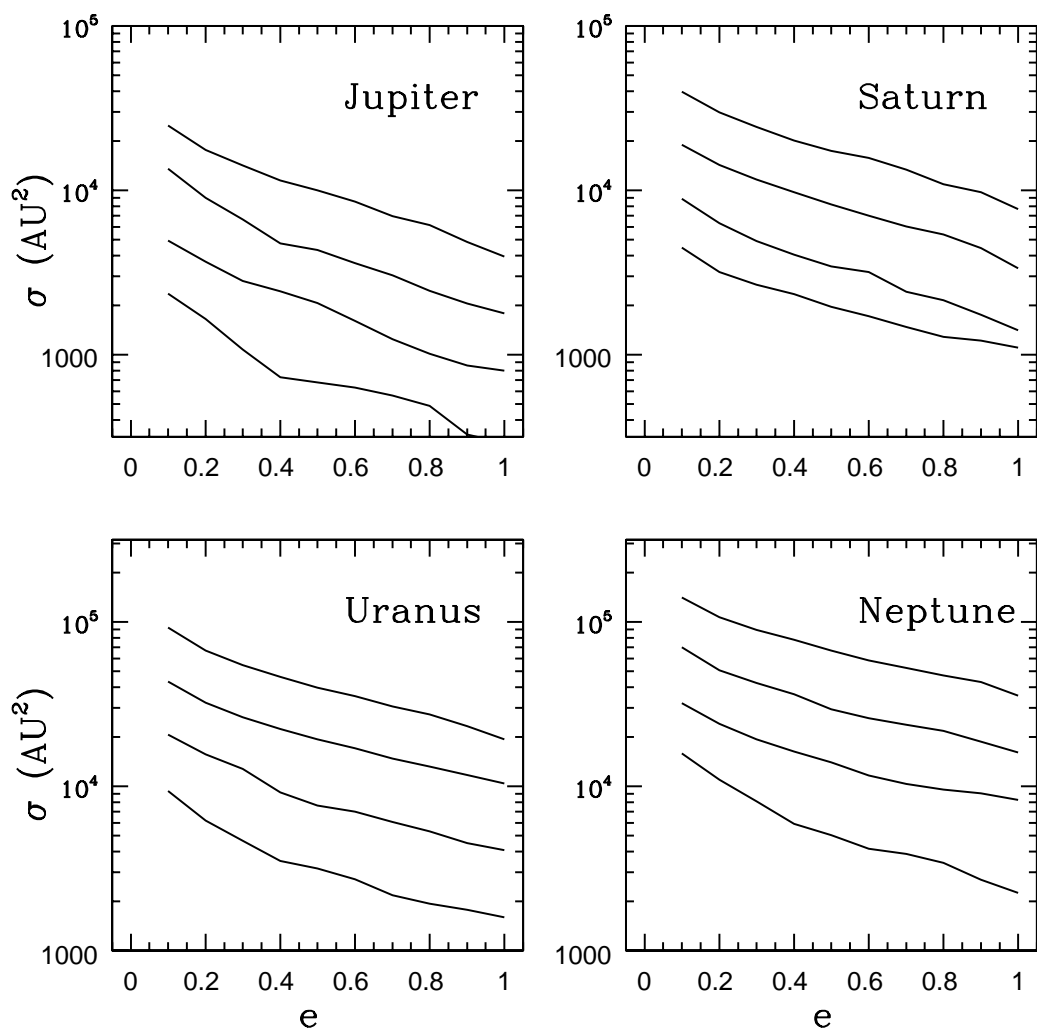
Fig. 11.— Cross sections for eccentricity increase due to encounters with passing single stars. The target systems are analogs of our Solar System, with the four giant planets in circular orbits with their current values of semimajor axis. Each panel shows the cross sections for a given planet, as labeled, where the curves correspond to varying velocity dispersions of the background cluster: $v_{\rm b} = 1, 2, 4$, and 8 km/s (from top to bottom).

Next we make a rough comparison of the cross sections for single star interactions (Figure 11) with those obtained earlier for binaries (e.g., Figure 3). The single star cross sections are smaller by *more than a factor of two*. Note that the binary systems are, on average, somewhat wider than the size of the solar systems. As a result, as a pair of stars passes by a solar system, it consists mostly of empty space but still provides (roughly) twice the opportunity for interaction as a single star. One thus expects at least a factor of two reduction in the cross sections for passing singles. The fact that the reduction is larger than a factor of two is thus significant and indicates that the dynamics of the binaries themselves must contribute. Further, as discussed in the following section, the cross sections for single stars exhibit a different dependence on the background velocity dispersion and a slightly steeper dependence on post-encounter eccentricity.

For convenience, Table 1 collects the cross sections for the ejection and capture of all four planets. For each solar system configuration considered in this paper, the table lists two sets of cross sections, where the first line corresponds to planetary ejection and the second line corresponds to planetary capture. The Standard Model (the first configuration in the table) represents the case where the four giant planets have the masses and semimajor axes of our current Solar System, the host star has mass $M_* = 1.0 M_\odot$, the velocity dispersion of the cluster $v_b = 1$ km/s, and the interacting stars are binary. The first column in the table labels the solar system configuration by the variable that differs from its standard value. The error bars in the table are those due to incomplete Monte Carlo sampling. One way to assess statistical significance is through the ratio of the cross section to its sampling error. For the ejection cross sections, the mean value (averaged over the entire table) of this signal to noise ratio is ~ 14, so that the ejection cross sections are well-determined. Capture events are much more rare. For the capture cross sections, the mean value of the signal to noise ratio is only ~ 4. For the rarest events, captures with high cluster velocity dispersion, the cross sections are only defined at the factor of two level.

4. Analysis and Scaling Laws

The cross sections found in the previous section display relatively simple dependences on the underlying variables of the problem: For example, for each type of solar system, the cross sections, when considered as functions of the post-encounter planetary eccentricity e, all display the same general shape. As a result, the functions $\langle \sigma \rangle (e)$ can (almost) be rescaled to find a universal functional form, where scaling factors take into account the initial semimajor axis a of the planet, the velocity dispersion v_b of the background environment, the stellar mass M_*, and so on. The goal of this section is to understand the general scaling properties of

the cross sections and to determine the extent to which they are self-similar. In general, self-similarity arises when physical scales are either missing from a problem or do not contribute to the results (Barenblatt 2003); we return to this issue at the end of the section.

Even in the reduced case where we consider one planet at at time, the interactions considered in this paper involve four bodies (the host star, the planet, and two binary members). Unfortunately, four-body interactions are rather difficult to describe analytically to any reasonable degree of approximation. As a result, the goal of this section is relatively modest: Instead of building complicated analytical models for 4-body (and higher N-body) dynamics, we consider here basic physical principles that can be used as motivation for scaling laws. We then combine these heuristic results with our detailed numerical determinations of the cross sections. The result is physically motivated fitting formula that characterize the cross sections over the parameter space of interest $(a, v_{\mathrm{b}}, M_*, e)$.

To start the discussion, consider the simplest case where the the cross section for interactions is the geometrical cross section πa^2 provided by a planet in its initial orbit. Further, we consider the planets to be independent of each other during the encounters. This cross section will be enhanced by gravitational focusing, so we can write down an heuristic expression for the cross section in the form

$$\langle \sigma \rangle_0 \approx \alpha \pi a^2 \left(1 + \frac{v_{esc}^2}{v_\infty^2} \right) , \tag{5}$$

where v_{esc} is the escape speed from the target system (at the location of the planet), and v_∞ is the asymptotic relative speed between the two systems. In order to pass within this cross sectional area, the interacting star (binary) must be about the same distance from the planet as its host star, so that the planet has a chance of being ejected from its original solar system. This expression thus represents the escape cross section. The parameter α is a dimensionless constant of order unity and is included to encapsulate the uncertainties inherent in this approximation. After inserting the expression for the escape speed, we obtain

$$\langle \sigma \rangle_0 = \alpha \pi a^2 \left(1 + \frac{GM_*}{a v_{\mathrm{b}}^2} \right) \rightarrow \alpha \pi \ell a , \tag{6}$$

where we have replaced the asymptotic speed v_∞ with the velocity dispersion v_{b} of the cluster (or other background stellar system) and we have defined the corresponding length scale $\ell \equiv GM_*/v_{\mathrm{b}}^2$ (where $\ell \sim 890$ AU for $v_{\mathrm{b}} = 1$ km/s). The final expression represents the limiting form, which is applicable when gravitational focusing dominates, and implies a linear dependence of the cross section on a. Given this form, the cross section requires another length scale. In this problem, the orbit speed of the binary, the asymptotic speed v_∞ of the encounter, the orbit speed of the planet, and the velocity dispersion v_{b} are all

roughly comparable (1 – 10 km/s). For example, the orbit of Neptune in our solar system has an escape speed of ~ 5.5 km/s, whereas the orbit speed of a binary at the peak of the period distribution is also ~ 5 km/s. If we only have a single velocity V, then dimensional analysis implies that the relevant length scale must be $\ell = GM_*/V^2$, as given in equation (6); additional uncertainties can be absorbed into the dimensionless parameter α. Finally we note that for a velocity dispersion $v_{\rm b} = 1$ km/s, the gravitational focusing term dominates by a factor of 30.

The limiting form of equation (6) is linear in the starting semimajor axis a of the planet. To see how well this expression works, we plot the ejection cross sections of the planets versus semimajor axis in Figure 12. As expected, the ejection cross section is a nearly linear function of the semimajor axis. This trend holds for solar systems starting with the present-day semimajor axes (star symbols) and the more compact configuration where the semimajor axes are spaced by factors of 5/3 (open triangles). We also plot results for ultra-compact solar systems in multiple mean motion resonance (open squares). In order to isolate the dependence of the cross sections on initial semimajor axis from planet-planet scattering effects, this latter case uses smaller planet masses (by a factor of 10), so they act more like test masses; to explore a wider range in a, we also take this compact system to be smaller by a factor of 1.35 compared to that considered in the previous section. The error bars delineate the uncertainty due to incomplete Monte Carlo sampling. Not only do the cross sections show nearly linear dependence on a, but the slope of the curve is predicted by the above analysis. The red solid (blue dashed) curve in Figure 12 shows the cross section predicted by equation (6) for the limiting case (full form); for both cases, the characteristic length scale $\ell = 890$ AU and the dimensionless parameter $\alpha = 7/5$.[*]

Next we consider the dependence of the cross sections on the post-encounter eccentricity e. For all four planets in all three types of solar system, the e-dependence is similar. Since the ejection cross sections scale linearly with semimajor axis a (see Figure 12), we scale the cross sections by dividing out one power of a. The resulting scaled cross sections are shown in Figure 13 as a function of eccentricity e. In addition to the individual cases (shown as the light dotted curves), the average is shown as the heavy blue curve, where the error bars depict the standard deviation. This latter quantity provides a measure of the spread in the values of the cross section over the various cases. The standard deviation varies from about 17% of the cross section at low eccentricity $e = 0.10$ to only about 9% at $e = 1.0$.

---

[*]In order to set the value for this dimensionless parameter, and others specified in this section, we generally search in increments of 10^{-2}, find the value that gives the minimum RMS error, and then choose the nearest round number (ratio of relatively small integers).
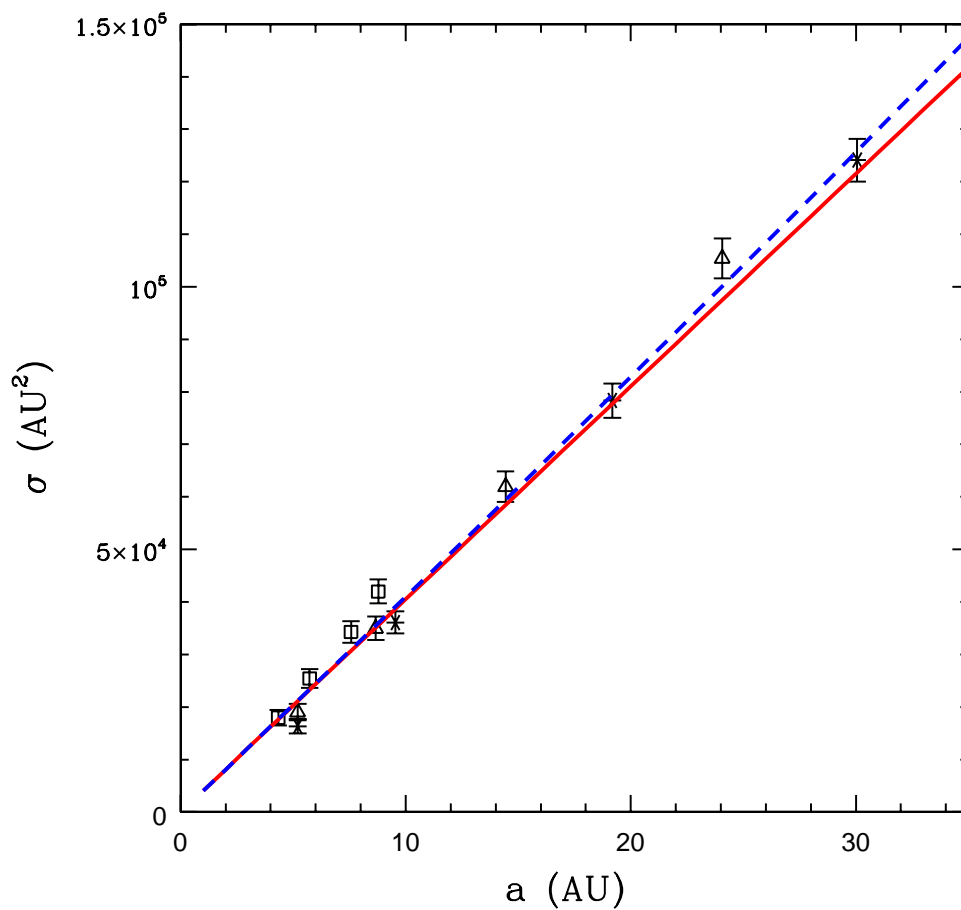
Fig. 12.— Cross sections for planetary escape versus the starting semimajor axis. The 12 points on the plot correspond to the four giant planets in each of three versions of the initial solar system architecture. The symbols represent different starting states, including the semimajor axes of the present-day solar system (stars), a compact configuration with 5/3 semimajor axis ratios (open triangles), and an ultra-compact solar system starting in multiple mean motion resonances (open squares). The red solid line shows the cross section indicated by the limiting form of equation (6); the blue dashed curve shows the full form.

The curves in Figure 13 are nearly straight lines on the semi-logarithmic plot, so that the dependence of the cross sections on eccentricity is nearly exponential. For purposes of illustration, we use an exponential fitting function of the form

$$\frac{\langle \sigma \rangle_e}{a} = \alpha \pi \ell \exp[\, b \, (1 - e)\,] \, , \tag{7}$$

where the first factor enforces consistency with the ejection cross sections considered above. For the value $b = 4/3$, we obtain a good fit to the calculated, scaled cross sections, as shown by the heavy red line in Figure 13. Except for first point ($e = 0.1$), the exponential fit (straight red line) agrees with the average values (solid blue curve) to within about 3%, i.e., the difference is much less than the width of the distributions as measured by the standard deviations. Another measure of the quality of the fit is provided the relative differences between the numerically determined cross sections used in constructing Figure 13 and the exponential form given by equation (7); the RMS of these relative errors is $\sim 12\%$.

Next we consider the effects of the velocity dispersion of the background cluster environment. As shown in Figure 3 in the previous section, the cross sections vary with the post-encounter eccentricity with approximately the same functional form over a wide range of $v_{\rm b}$. Only the leading cofficient changes. Moreover, the uniform spacing of the curves in Figure 3 indicates that the cross sections must have a power-law dependence on the velocity dispersion $v_{\rm b}$ (to leading order). We have explored scalings with velocity dependence of the form $\langle \sigma \rangle \propto v_{\rm b}^{-\gamma}$ and find that the best fit occurs for $\gamma \approx 7/5$. Using this choice of power-law index, we plot the scaled cross sections versus post-encounter eccentricity in Figure 14, where we include the linear a-dependence found previously (i.e., $\langle \sigma \rangle v_{\rm b}^{7/5}/a$). Each light dotted curve in the figure shows the result for one planet and one choice of velocity dispersion. The heavy blue curve shows the average over all of the curves, where the error bars depict one standard deviation. The heavy straight red line represents the same exponential dependence given in equation (7) and used in Figure 13. The RMS of the relative differences between the numerically determined cross sections and the curve given by equation (7) is $\sim 13\%$. The cross section curves are thus self-similar to this level of accuracy. Furthermore, the dependence of the cross sections on velocity dispersion is nearly independent of the dependence on starting semimajor axis a of the planet.

The dependence of the interaction cross sections on the mass of the host star is somewhat more complicated than for the other variables, as illustrated in Figure 4. As the mass M_* of the star increases, the cross sections, considered as functions of eccentricity, become steeper. The spacing of the curves in Figure 4 (for different stellar masses) grows with e, so that the curves are not self-similar. In spite of this complication, we can still fit the cross sections with a power-law function of stellar mass, although the accuracy of the approximation is not expected to be as high as in the previous cases. We thus consider a scaling of the form

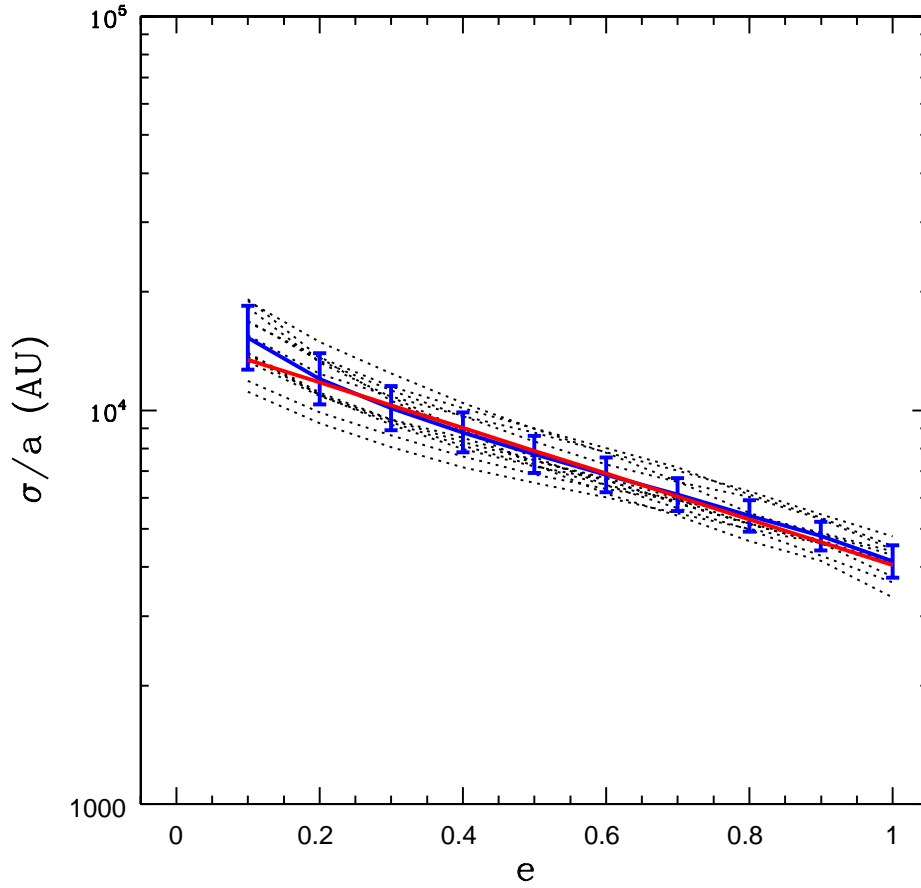Fig. 13.— Scaled cross sections versus the post-encounter eccentricity e for the four giant planets in each of the starting architectures for the solar system. The individual cases are shown as light dotted curves. The heavy solid blue curve depicts the average, where the error bars depict the standard deviation. The straight red line shows the result for cross sections with a purely exponential dependence on eccentricity.

Fig. 14.— Scaled cross sections versus the post-encounter eccentricity e for a collection of different velocity dispersions for the background. The starting state is taken to have four giant planets with the current semimajor axes. Cross sections are scaled by $v_{\rm b}^{7/5}/a$ (see text). The individual cases are shown as light dotted curves, with include curves for each of the planets for $v_{\rm b} = 1 - 16$ km/s, equally spaced logarithmically (by factors of $\sqrt{2}$). The heavy solid blue curve depicts the average, where the error bars depict the standard deviation. The red striaght line shows the result for cross sections with a purely exponential dependence on eccentricity.
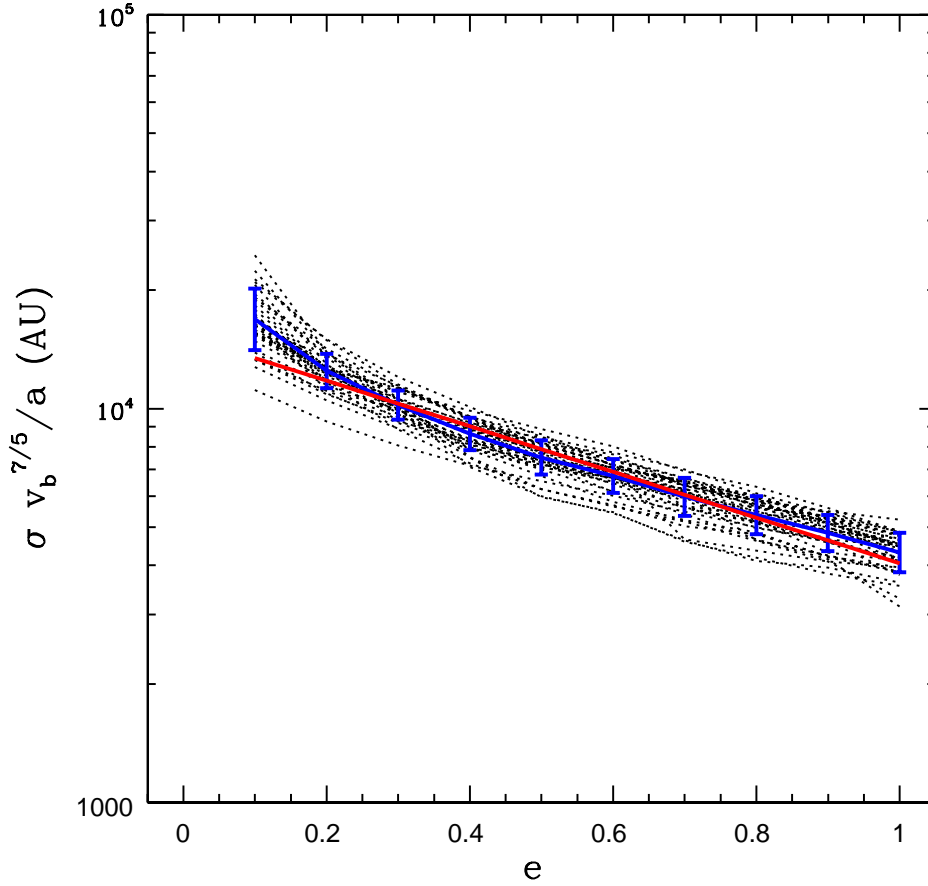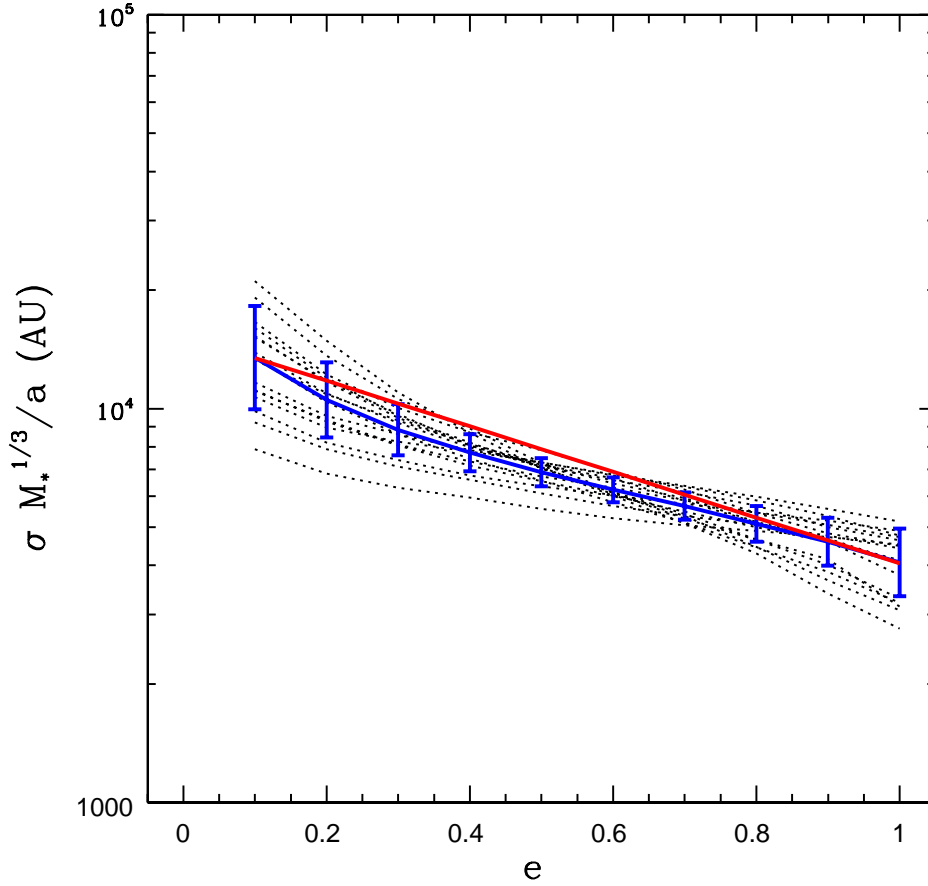
Fig. 15.— Scaled cross sections versus the post-encounter eccentricity e for solar systems with different stellar masses. The starting state is taken to have four giant planets with the current masses and semimajor axes. Cross sections are scaled by $M_*^{1/3}/a$ (see text). The individual cases are shown as light dotted curves, with include curves for each of the four planets for four choices of stellar mass $M_* = 0.25 - 2.0\ M_\odot$ (spaced by factors of 2). The heavy solid blue curve depicts the average, where the error bars depict the standard deviation. The red striaght line shows the result for cross sections with a purely exponential dependence on eccentricity.

$\langle\sigma\rangle \propto M_*^{-\mu}$, and vary the index μ to find the best fit. The choice $\mu = 1/3$ provides the lowest RMS of the relative error. Figure 15 shows the result by plotting the scaled cross sections $\langle\sigma\rangle M_*^{1/3}/a$ (again including the linear dependence on semimajor axis a) as a function of post-encounter eccentricity. The light dotted lines show the individual (scaled) cross sections and the heavy blue curve shows the average. The error bars depict the corresponding standard deviation, which is larger than for the cases considered previously (compare Figure 15 with Figures 13 and 14). The heavy red staight line shows the same result as before (from equation [7]). The RMS error between the exponential line and the numerically determined cross sections is about 20%. This larger error measure results from fitting the cross sections with a power-law form, even though the results depart somewhat more from self-similarity.

The cross sections for increasing the spread of inclination angles, considered over a range of velocity dispersions, also show a nearly self-similar form (see Figure 7). This finding indicates that the cross section should scale with a nearly power-law dependence so that $\langle\sigma\rangle \propto v_{\mathrm{b}}^{-\eta}$. Over the range $v_{\mathrm{b}} = 1 - 16$ km/s, we find that the best fit occurs for $\eta \approx 7/5$. To illustrate how well this scaling law works, we plot the scaled cross sections $\langle\sigma\rangle v_{\mathrm{b}}^{7/5}$ as a function of $\sin(\Delta i)$ in Figure 16. Each light dotted curve in the figure corresponds to the result of one choice of velocity dispersion. The heavy blue curve shows the average of the scaled cross sections, where the error bars depict the standard deviations. The mean size of the error bars corresponds to relative differences of $\sim 6\%$, so that the curves are self-similar to this degree of accuracy. Notice that the scaling exponent $\eta \approx 7/5$ for inclination angle increases as a function of velocity dispersion v_{b} is the same as the corresponding index for eccentricity increases.

After the velocity dependence has been scaled out, the cross section for increasing the spread of inclination angles is a slowly varying monotonic function of Δi (see Figure 16). If we consider $x = \sin \Delta i$ as the independent variable (instead of Δi itself), the cross section can be fit with an exponential function which is analogous to that used to describe the eccentricity dependence. More specifically, if we use the functional form

$$\langle\sigma\rangle_i = \langle\sigma\rangle_0 \exp\left[b_0 \left(1 - \sin \Delta i\right)\right] , \tag{8}$$

then the cross section for increasing Δi can be fit using the parameters $b \approx 3/4$ and $\sigma_0 \approx 166{,}000$ AU^2. Note that the value of the index b used here somewhat smaller than that needed to fit the dependence of the cross sections on (post-encounter) eccentricity (compare with equation [7]). The fitting function from equation (8) is shown in Figure 16 as the solid red curve. The quality of the fit is reasonably good: The fitting curve falls within one standard deviation (marked by errorbars in the figure) of the mean for all of the range except the first point ($x = \sin \Delta i = 0.1$); alternately, the RMS of the relative error between the two curves is $\sim 8\%$. However, the mean of the numerical results (blue curve) shows more
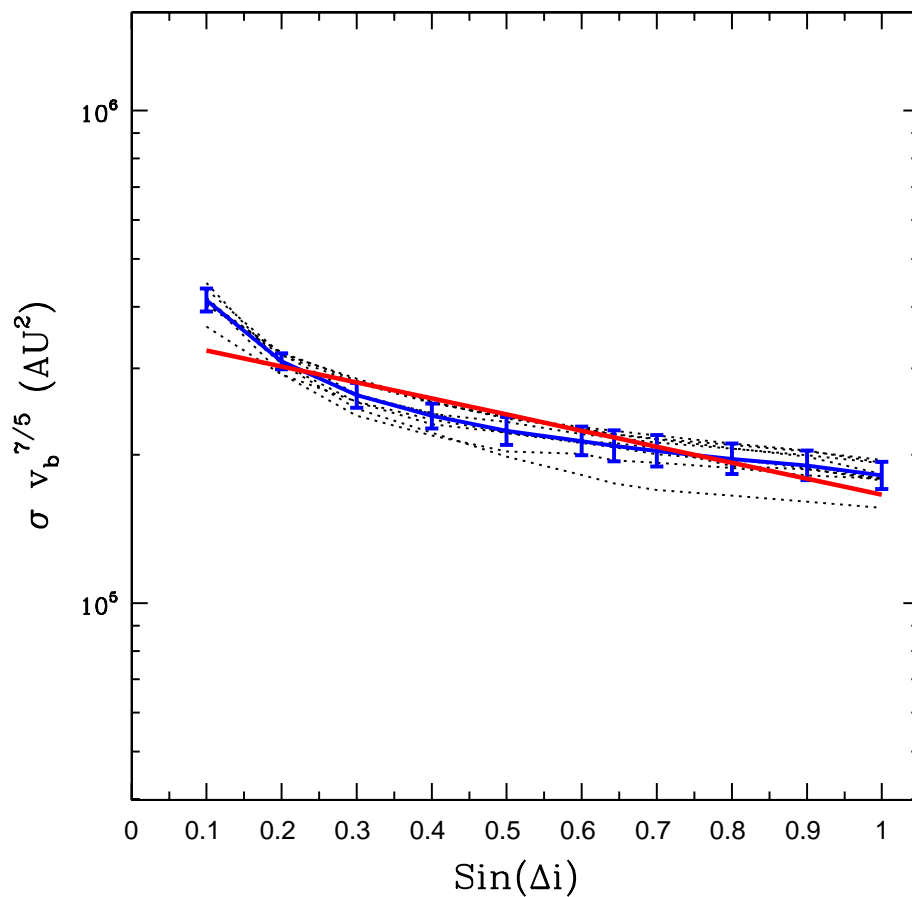
Fig. 16.— Scaled cross sections for increasing the post-encounter spread Δi of the inclination angles of the planetary orbits. The starting states have the four giant planets orbiting in the same plane ($\Delta i = 0$). The cross sections are scaled by the velocity dispersion of the cluster with the relation $\langle\sigma\rangle v_{\rm b}^{7/5}$. The individual cases are shown as light dotted curves. The heavy solid blue curve depicts the average, whereas the error bars depict the standard deviation. The heavy red curve shows the fitting function described in the text.

curvature than the exponential fit (red curve), especially at small values of x.

Although we could find a more complicated fitting function that has smaller RMS relative error, we use equation (8) in order to compare changes in the spread of inclination angle with changes orbital eccentricity. If we equate the variable $x = \sin \Delta i$ with e, then equations (7) and (8) have the same general form. We can then compare the leading coefficients, which have values $\langle \sigma \rangle_0 \approx 166{,}000$ AU^2 for Δi-dependence and $\alpha \pi \ell a \approx 120{,}000$ AU^2 for e-dependence, where we have used $a = 30$ AU to evaluate the latter expression. The cross sections for eccentricity increase and spread of the inclination angles thus display similar behavior. The leading coefficients agree to within $\sim 28\%$ and we can make the following inexact analogy: An increase in Neptune's eccentricity of $\Delta e = 0.1$ corresponds to changing the spread of the inclination angles (of all four planets) so that $\sin \Delta i$ increases by 0.1. We can also make a rough association between increasing the spread of inclination angles to $\Delta i \geq 90$ degrees and the ejection of a planet ($e \geq 1$). Both of these events have (approximately) the same cross section and both involve order unity changes to the angular momenta of the planetary orbits. In addition, the cross sections for inclination angle increase and eccentricity increase scale with the velocity dispersion in the same manner ($\propto v_{\rm b}^{7/5}$).

The association between changes in the variables $\sin \Delta i$ and e provides an intriguing topic for additional work. To leading order, the canonical actions written in terms of the orbital elements have the forms

$$\Gamma \propto \frac{1}{2} e^2 \qquad \text{and} \qquad Z \propto \sin^2(i/2) \, . \tag{9}$$

The apparent relation between the two variables (as observed in the simulation results) could thus be evidence of an equipartition-like mixing of the actions (see Lichtenberg & Lieberman 1992). Although beyond the scope of the present paper, this issue should be explored further.

We can extract a potentially important cross section from these results. The scattering interactions considered here can readily increase the spread of inclination angles of outer bodies in a solar system. On the other hand, the scattering events themselves have little effect on planets in tight orbits, such as the multi-planet systems observed by the *Kepler* mission (Batalha et al. 2013). However, the bodies in the outer solar system can have important long-term effects on the inner bodies provided that they are scattered into orbits with sufficiently high inclination angles. More specifically, if the inclination angles of the outer orbits are larger than 39.2°, then the Kozai effect can operate (Kozai 1962; Lidov 1962), and the inner portions of the solar system can be excited over the age of the systems. Combining this requirement with the results of our numerical simulations, we find that the cross section for scattering a solar system into a state where the Kozai effect can operate is

given by

$$\langle\sigma\rangle_{\text{kozai}} \approx 210,000\,\text{AU}^2 \left(\frac{a_{\text{out}}}{30\,\text{AU}}\right)\left(\frac{v_{\text{b}}}{1\,\text{km/s}}\right)^{-7/5}, \qquad (10)$$

where a_{out} is the semimajor axis of the outermost planet of the system. Note that the requirement of large mutual inclination is necessary but not sufficient for the Kozai effect to play a role. The Kozai effect is a highly fragile type of interaction because it involves libration of the argument of periastron, and this quantity can be subject to many other sources of precession (for further discussion, see Batygin et al. 2011). We also note that this form for the cross section (equation [10]) involves some extrapolation: The numerical simulations were carried out primarily for the architecture of the current solar system. Nonetheless, the outermost planet is always the most affected by fly-by interactions, and the cross sections scale linearly with semimajor axis to a good approximation.

Next we consider the scaling behavior of the cross sections for interactions with passing single stars. As for the case of binary systems, we expect the cross sections to scale nearly linearly with the semimajor axis a of a given planet. In addition, the nearly equal spacing on the logarithmic plot of Figure 11 indicates that the cross sections should display power-law dependence on the velocity dispersion, such that $\langle\sigma\rangle \propto v_{\text{b}}^{-\gamma_s}$. The velocity dependence for these single star cross sections is moderately less steep than those found earlier for binaries; the optimal value of the index $\gamma_s \approx 6/5$, which is somewhat smaller than the value for binary cross sections $\gamma \approx 7/5$. After scaling out the semimajor axis and velocity dispersion, the reduced cross sections are shown in Figure 17. The light dotted curves show the scaled values for given planets and values of v_{b} (which lie in the range $1-8$ km/s). The heavy blue curve shows the mean over the entire collection and the error bars denote the standard deviations. These error bars correspond to an average relative error of $\sim 15\%$, which is comparable to, but somewhat larger than that found for the binary cross sections.

The scaled cross sections shown in Figure 17 for single star interactions show a nearly exponential dependence on the post-encounter eccentricity. Although this behavior is analogous to that found for the binary cross sections, the slope of the exponential is somewhat steeper. Here we consider a fitting function of the form

$$\langle\sigma\rangle_{\text{single}} = \langle\sigma\rangle_0 \left(\frac{a}{\text{AU}}\right)\left(\frac{v_{\text{b}}}{1\,\text{km/s}}\right)^{6/5} \exp\left[b_s(1-e)\right], \qquad (11)$$

where we obtain a good fit for $\langle\sigma\rangle_0 = 1000\,\text{AU}^2$ and $b_s = 8/5$. The resulting fit is shown as the red straight line in Figure 17. The RMS difference between the expression of equation (11) and the numerically determined, scaled cross sections for single stars is only $\sim 8\%$.

Now we can compare the cross sections for single stars with those for binaries. The comparison is complicated by the different scalings of the two cases with velocity dispersion
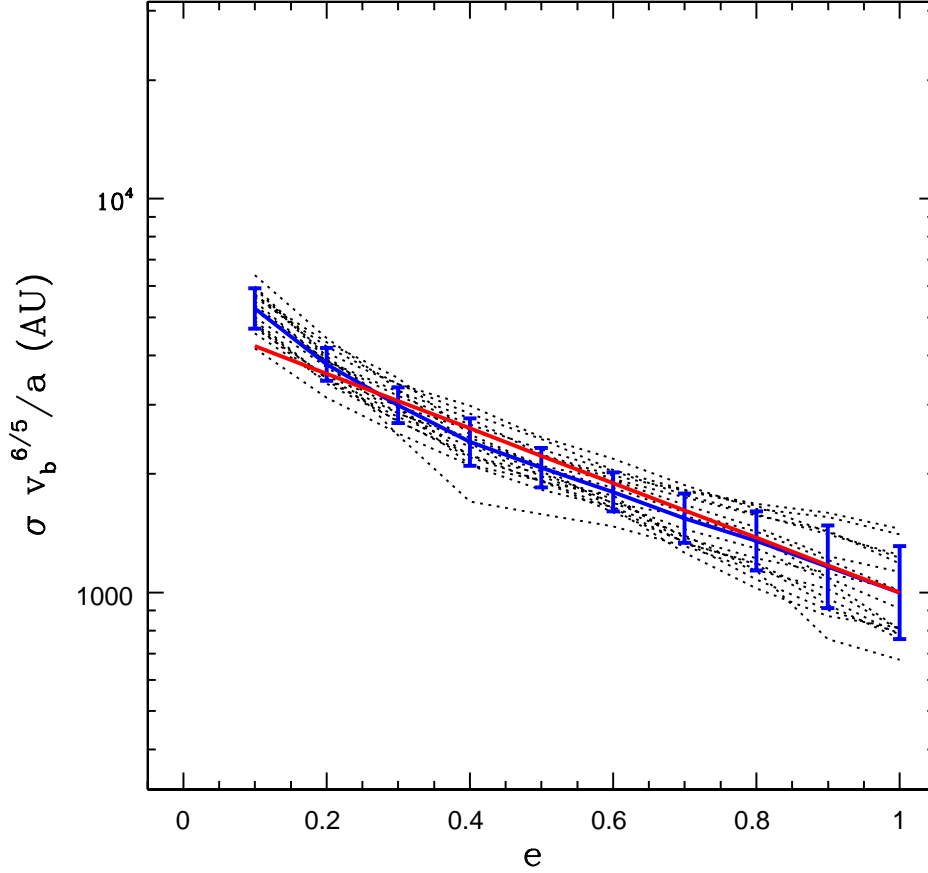
Fig. 17.— Scaled cross sections versus the post-encounter eccentricity e for solar systems interacting with single stars. The starting states have four giant planets with the current masses and semimajor axes of our Solar System. Cross sections are scaled by the factor $v_{\rm b}^{6/5}/a$. The individual cases are shown as light dotted curves, which include the four giant planets and four values of velocity dispersion of the background cluster: $v_{\rm b} = 1, 2, 4,$ and 8 km/s. The heavy solid blue curve depicts the average, where the error bars depict the standard deviation. The red striaght line shows the result for cross sections with an exponential dependence on eccentricity.

and the different exponential laws for the eccentricity dependence. To fix ideas, consider the benchmark case where the velocity dispersion $v_{\rm b} = 1$ km/s for the background cluster. Here, the cross sections for binary star interactions are ~ 4.2 times larger than those for single stars at the high end of the eccentricity range $e = 1$. Similarly, the binary cross sections are ~ 3.2 times larger at the low end of the eccentricity range where $e = 0.10$. Averaged over the span of eccentricity considered here, the binary cross sections are larger by a factor of ~ 3.6. This factor decreases with increasing velocity dispersion, however, because the binary cross sections fall according to the relation $\langle \sigma \rangle \propto v_{\rm b}^{-7/5}$, whereas the single star cross sections fall as $\langle \sigma \rangle \propto v_{\rm b}^{-6/5}$. With these scaling laws, the cross sections for binaries are only a factor of 2 larger (than those for single stars) when the velocity dispersion is increased to $v_{\rm b} \approx 20$ km/s.

These results can be interpreted as follows: At high asymptotic speeds, which occur for $v_{\rm b} \gtrsim 20$ km/s, the two members of a binary pass by the solar system quickly enough so that binary motion and planetary motion play only a minor role in the interaction (this speed is much larger than the mean orbital speed of either the binary or the outer planet). As a result, the two stars interact with the solar system in an almost independent manner, and the cross sections for binary interactions should be a factor of ~ 2 larger than those for single stars (for large $v_{\rm b}$). On the other hand, lower impact speeds can be comparable to the binary orbital speed and/or the planetary orbital speeds. In this regime, the motion of the binary stars relative to one another during the encounter can increase their chances of interacting with the planets, thereby leading to larger cross sections. In extreme cases, resonant interactions can occur when the velocity scales of the problem are all comparable (see also Laughlin & Adams 2000), and these long-lived events can greatly increase the chances of disruption of planetary orbits during the encounters. To be consistent with this picture, the ratio of the single-star cross section to the binary cross section must decrease less steeply with $v_{\rm b}$, as found here.

Before leaving this section, we briefly address the issue of how self-similarity can arise in the context of solar system scattering. In its full form, this problem has six velocities (four planetary orbits, one binary orbit, and the encounter velocity) and seven masses (four planets and three stars). One expects self-similarity only when most of these scales do not contribute (Barenblatt 2003). We can construct an argument to reduce the number of relevant scales as follows: To leading order — and only during the encounter itself — planetary interactions with the binary are independent of interactions with other planets. As a result, we can (often) treat the encounters as single-planet systems scattering with binaries. The planet itself is usually small enough to be considered as a test mass, so that we are left with "only" three masses and three velocities. The binary masses are always drawn from the same IMF, and the cross sections are determined through many samples of that IMF ($\mathcal{N}_E \gtrsim 80,000$), thereby leaving the ratio $M_*/(M_{1*} + M_{2*})$ as the most important mass variable. In the regime

of interest, the cross sections have values in the range $\langle \sigma \rangle \sim 10^4 - few \times 10^5$ AU^2, which implies that the length scales that characterize the interactions $\ell_c \equiv \langle \sigma \rangle^{1/2} \approx 100 - 500$ AU. This size scale is larger than that of both the planetary orbits ($a = 5 - 30$ AU) and most binary orbits (where the peak of the period distributions corresponds to $a_b \approx 42$ AU). If the orbital speeds of the planets and the binary are fast enough, then their orbits can be replaced by rings of mass with the same semimajor axis and eccentricity (Murray & Dermott 1999). This averaging effectively eliminates the orbital velocities from the problem and leaves the velocity dispersion v_b as the most important velocity variable. Indeed, we find that the cross sections depend most sensitively on the stellar host mass M_* (equivalently, the mass ratio $M_*/(M_{1*} + M_{2*})$) and the velocity dispersion v_b. This argument is not exact, however, and the additional scales (e.g., orbits speeds) do play some role. These complications are responsible for the spread in the scaled cross sections shown in Figures 12 – 16.

5. Application to the Solar Birth Aggregate

Given that most stars are born within clusters, it is likely that the birth environment of our own Solar System was a cluster of some type. The argument for a substantial birth cluster is bolstered by evidence for short-lived radionuclides in meteorites, which suggests that the early solar nebula was enriched by a nearby supernova (Cameron & Truran 1977; see the review of Dauphas & Chaussidon 2011). A number of previous papers have considered how dynamical scattering encounters in this putative birth cluster can provide constraints on the cluster properties (see the discussion of Section 1). Unfortunately, however, no consensus has been reached. This section briefly revisits the issue in light of the updated cross sections determined above.

The basic problem posed by the solar birth aggregate involves a number of ingredients: [I] Direct supernova enrichment of the early solar nebula requires a nearby massive star, which is more likely to form in a larger stellar system. Further, significant nuclear enrichment requires close proximity (distances $d = 0.1 - 0.3$ pc), which implies that the supernova progenitor lives within the same cluster. Acting in the opposite direction, larger clusters can potentially disrupt planetary systems through the action of both [II] dynamical scattering (with the cross sections determined here) and through [III] intense radiation fields which can evaporate gaseous disks. In order for the solar system to reach its present-day state, however, the orbits of the giant planets cannot be greatly perturbed and the early solar nebula could not be too severely evaporated. On the other hand, [IV] the classical Kuiper belt has an apparent edge at ~ 50 AU, and [V] the dwarf planet Sedna has an unusual orbit; both of these solar system properties could be explained by *requiring* a close encounter with another

member of the cluster. The challenge is to find a birth scenario for the solar system that successfully negotiates the compromises required to simultaneously explain all five of these constraints. Supernova enrichment, the edge of the Kuiper belt, and the orbit of Sedna all argue in favor a large and long-lived cluster; disruption via both scattering and radiation argue in the opposite direction.

Existing work has considered a variety of approaches to this issue. Several authors advocate solar birth clusters with stellar membership size in the range $N = 10^3 - 10^4$ (e.g., Adams & Laughlin 2001; Portegies Zwart 2009; Adams 2010; Pfalzner 2013). These studies find that cluster systems in this decade of N lead to moderate dynamical disruption of their constituent planetary systems. Additional work focuses on even larger, longer-lived clusters and find that they can instigate substantial changes to planteary orbits, including frequent ejections (Malmberg et al. 2007, 2011; Spurzem et al. 2009; Parker & Quanz 2012; Hao et al. 2013). On the other hand, competing work suggests that the solar birth cluster does not produce significant disruption of planetary orbits (Williams & Gaidos 2007; Dukes & Krumholz 2012; Craig & Krumholz 2013; see also Williams 2010).

The aforementioned papers thus reach different conclusions about the importance of dynamical scattering of planetary systems in clusters. These differences arise because of varying assumptions about cluster properties and varying assumptions about how to enforce the five constraints on solar system properties outlined above. Although a full review of this topic is beyond the scope of this work, we provide a brief overview below (for additional detail, see the reviews of Adams 2010; Dauphas & Chaussidon 2011; Pfalzner 2013).

For a given type of disruption, with cross section $\langle\sigma\rangle$, the interaction rate is given by $\Gamma = n_*\langle\sigma\rangle v$ (from equation [1]). The total expected number N_{dis} of disruption events, per solar system, integrated over the lifetime τ of the cluster is then given by

$$N_{\mathrm{dis}} = \int_0^\tau \Gamma dt = \int_0^\tau n_*\langle\sigma\rangle v dt \,. \tag{12}$$

The number of disruptive interactions thus depends on the speed v at which a given solar system encounters passing binaries, their number density n_*, and the total time τ spent within the cluster.

We first consider the speed v. Recall that the interaction cross section $\langle\sigma\rangle$ varies with the velocity dispersion of the cluster according to the relation $\langle\sigma\rangle \propto \langle\sigma\rangle_0 v_{\mathrm{b}}^{-7/5}$. If we identify the speed v with the velocity dispersion v_{b} of the cluster, then the product $\langle\sigma\rangle v \propto v_{\mathrm{b}}^{-2/5}$. As a result, most of the velocity dependence of the cross section is compensated by that of the interaction rate, so that the number of disruption events depends only weakly on the velocity dispersion. As an example, consider the Orion Nebula Cluster (ONC), an intermediate-sized young stellar system with velocity dispersion $v_{\mathrm{b}} \sim 2$ km/s (Hillenbrand & Hartmann 1998).

Provided that it stays intact, the ONC is likely to evolve into an open cluster resembling the Pleiades (Kroupa et al. 2001); over the coming ~ 100 Myr, the velocity dispersion of the cluster will slowly decrease to $v_{\rm b} \sim 1$ km/s. Over this span of time, the quantity $v_{\rm b}^{-2/5}$ that defines the velocity dependence of the interaction rate varies by only about 32%.

For setting the number of disruption events, one important quantity is the time τ over which clusters remain intact as dynamical systems. In the simplest terms, although most stars are formed in clusters, these astronomical entities come in (at least) two distinctly different flavors. Only about 10 percent of the stellar population is born within clusters that are sufficently robust to become open clusters (Roberts 1957; Battinelli & Capuzzo-Dolcetta 1991), which are relatively long-lived ($\tau = 100$ Myr – 1 Gyr). The remaining 90 percent of the stellar population is born within embedded clusters (e.g., Allen et al. 2007), which have much shorter lifetimes ($\tau \sim 10$ Myr). As shown below, solar systems that are born within long-lived clusters can have an appreciable chance of dynamical disruption; short-lived clusters lead to significant disruption with greatly reduced probability.

Another important quantity is the density of the cluster. For clusters found in the solar neighborhood, the cluster radius $R \propto N^{1/2}$ (Lada & Lada 2003), so that the clusters display nearly constant surface density (Adams et al. 2006). With this relation, clusters with larger stellar membership sizes N have lower mean densities. However, the clusters in the sample are relatively small (with $N < 2500$), and this trend does not continue up to the largest clusters with $N = 10^4 - 10^6$ (Whitmore et al. 2007), or to the subpopulation of systems that become globular clusters. The largest clusters can thus have larger densities.

To assess the effects of scattering encounters, we need to specify the rate Γ at which solar systems encounter passing binaries (and single stars). As shown previously (Adams et al. 2006; Proszkow & Adams 2009), the rate of close encounters in a cluster can be written in the convenient form

$$\Gamma = \Gamma_0 \left(\frac{b}{b_0} \right)^{\gamma} , \tag{13}$$

where b_0 is a fiducial distance (taken here to be $b_0 = 1000$ AU), and where the fiducial rate Γ_0 and index γ depend on the cluster properties. The index γ falls in the range $1 \le \gamma \le 2$, where the extreme of the range correspond to perfect gravitational focusing ($\gamma \to 1$) and the full geometrical cross section ($\gamma \to 2$). In these systems, encounters beyond ~ 1000 AU are little affected by gravitational focusing. Since the cross sections calculated in this paper include gravitational focusing, we can write the interaction rate in the form

$$\Gamma = \Gamma_0 \frac{\langle \sigma \rangle}{\pi b_0^2} . \tag{14}$$

The benchmark interaction rate Γ_0 has a typical value of about 0.1 interactions per target

star per Myr. However, given the wide range of possible cluster properties, it can vary over a wide range, from an order of magnitude lower to an order of magnitude larger than this fiducial value (see Figures 6 and 7, and Tables 8 – 13 in Proszkow & Adams 2009). Note that the benchmark rate is, in general, larger than the simple estimate $\Gamma_0 \sim \langle n_* \rangle v_b \pi b_0^2$, where $\langle n_* \rangle$ is the mean density of the cluster. The stellar density that defines the interaction rate is not the mean over the cluster, but rather the weighted mean over the integrated orbits of the ensemble of cluster members. The cluster members generally do not stay at a given cluster radius, and the cluster density is centrally concentrated, so that solar systems sample the higher stellar densities of the cluster core. This effect is amplified by the starting conditions for clusters, which start with subvirial initial conditions; as a result, the orbits are more radial than isotropic, resulting in more excursions through the dense central core (see Adams et al. 2006; Proszkow & Adams 2009 for further discussion).

Collecting the results outlined above, we can write the number of disruption events (from equation [12]) in the form

$$N_{\text{dis}} \approx \frac{\langle \sigma \rangle_0}{\pi b_0^2} \int_0^\tau \Gamma_0 \left(\frac{v_b}{1\,\text{km/s}} \right)^{-2/5} dt \,. \tag{15}$$

The cross section for moderate solar system disruption can be taken as $\langle \sigma \rangle_0 \approx 2.5 \times 10^5\ \text{AU}^2$, which corresponds to events producing eccentricity increases $\Delta e = 0.1$ and/or increases in the spread of inclination angles $\Delta i = 10°$ (e.g., see Figures 1 and 7). To obtain this value, we use a linear combination of the binary and single-star cross section (see Figure 11), and an assumed binary faction of 2/3. Although these changes to the orbital elements are not devastating, they are large enough to distinguish a disrupted solar system from our own. Note that this value can be written $\langle \sigma \rangle_0 \approx (500\,\text{AU})^2$, which is somewhat larger than the previous estimate of $\sim (400\,\text{AU})^2$ (from Adams & Laughlin 2001).[†] The leading factor in equation (15) is thus of order 1/10. Since the benchmark interaction rate $\Gamma_0 \sim 0.1\ \text{Myr}^{-1}$, the cluster lifetime must be relatively long, $\tau \sim 100$ Myr, in order for disruption to take place with high probability. In other words, most solar systems residing in long-lived clusters can experience moderate disruption.

The cross sections for planet ejection are smaller than the values used above by a factor of ~ 3. As a result, only a fraction ($\sim 1/3$) of the solar systems in long-lived clusters are expected to lose planets with Neptune-like orbits (with even smaller fractions for closer

---

[†]The difference arises because the present study increases the target area in equation (2) from $B = 4$ to $B = 100$, thereby including more distant events. Note that the original work (Adams & Laughlin 2001) correctly introduced the cross sections as lower limits. The present cross sections are also lower limits, although they are much closer to their greatest lower bounds.

planets). Keep in mind, however, that the benchmark interaction rates Γ_0 can vary by a factor of ~ 10 in both directions.

The above considerations resolve some of the differences found in the literature concerning the disruption rates for planetary systems in clusters. In order for disruption to occur with high probability, clusters must live for relatively long times $\tau \gtrsim 100$ Myr. Indeed, the studies that find low disruption rates consider the clusters to have relatively short lifetimes $\tau \sim 10$ Myr (e.g., Williams & Gaidos 2007; Dukes & Krumholz 2012).

How long are clusters expected to stay together? As outlined above, the cluster population has at least two branches. Some clusters disperse over relatively short time scales of only ~ 10 Myr. The robust clusters that survive to become open clusters have empirically determined lifetimes τ_{em} that can fit with a function of the form

$$\tau_{em} = 2.3 \text{Myr} \left(\frac{M_c}{1 M_\odot} \right)^{0.6} , \tag{16}$$

where M_c is the cluster mass (Lamers et al. 2005). With this relation, clusters with initial masses larger than $\sim 550 M_\odot$ live longer than 100 Myr and can potentially disrupt their constituent solar systems. More specicifally, we can write the dynamical constraint in the form

$$N_{\text{dis}} \approx \frac{\langle \sigma \rangle_0}{\pi b_0^2} \langle \Gamma_0 \rangle 2.3 (\Upsilon N)^{3/5} \langle (v_{\text{b}}/1 \, \text{km/s})^{-2/5} \rangle \lesssim 1 , \tag{17}$$

where Υ ($\approx 1/2 \, M_\odot$/star) is the mass-to-number ratio (the conversion factor between cluster mass M_c and cluster membership size N), and where we include the time average of the velocity dispersion of the cluster (raised to the proper power). After some rearrangement and the specification of typical numbers, this constraint can be written in the form

$$N \lesssim 5000 \left[\left(\frac{\langle \sigma \rangle_0}{2.5 \times 10^5 \text{AU}^2} \right) \left(\frac{\langle \Gamma_0 \rangle}{0.05 \text{Myr}^{-1}} \right) \left\langle \left(\frac{v_{\text{b}}}{1 \, \text{km/s}} \right)^{-2/5} \right\rangle \right]^{-5/3} \lesssim 10^4 . \tag{18}$$

Note that the disruption cross section is determined more precisely than either the expected age of the cluster (from equation [16]) or the benchmark interaction rate Γ_0. This latter quantity can be determined to high accuracy for a given set of cluster properties and initial conditions, but its value varies appreciably from cluster to cluster (Proszkow & Adams 2009). Equation (18) uses a value near the low end of the range in order to provide an upper limit on N. In light of these uncertainties, a reasonable order-of-magntidue estimate for the dynamical constraint is $N \lesssim 10^4$, as given by the final inequality. This result is roughly consistent with previous estimates (Adams & Laughlin 2001; Portegies Zwart 2009; Adams 2010; Pfalzner 2013). Nonetheless, the full probability distribution for the survival (or disruption) of planetary systems as a function of cluster size N should be constructed.

The constraint given by equation (18) assumes that the solar birth cluster is relatively long-lived. If the solar system formed within a cluster that disperses in only ~ 10 Myr, the corresponding dynamical constraint would be considerably weaker. The motivation for considering a long-lived cluster comes from constraints jointly implied by the five solar system properties outlined at the beginning of this section. Direct supernova enrichment [I] favors a long-lived cluster, so that the progenitor star has enough time to live, evolve, and explode. An even stonger argument comes from the need for a scattering event to produce the edge of the classical Kuiper belt [IV] and to produce the orbit of Sedna [V]. If these solar system properties arise from dynamical interactions in the birth cluster, then a long-lived stellar system is strongly indicated. It remains possible for these features of the solar system to be explained in other ways. Nonetheless, any self-consistent set of constraints on the solar birth environment must explain all three of these properties, and must simultaneously account for the corresponding constraints due to dynamical scattering encounters [II] and radiation fields [III] (e.g., see Fatuzzo & Adams 2008; Thompson 2013).

For completeness, we also consider possible constraints on the solar birth cluster for the scenario where the solar system spends much of its early life in the ultra-compact multi-resonant configuration (see Section 3, Figure 2). The cross section for removing the solar system from its resonant state is then given by equation (3), which is more than nine times larger than that used above. If, in addition, the removal of the solar system from resonance *always* led to significant disruption over longer times, then the maximum size of the solar birth cluster would be ~ 40 times smaller than that of equation (18). In practice, however, the solar system, after being removed from resonance, will not always be significantly disrupted (for example by ejecting a planet) before it evolves and spreads out (as advocated by the Nice model; Gomes et al. 2005; Tsiganis et al. 2005). To assess the risk of disruption in this case, one must also know the probability of the non-resonant (but still compact) solar system experiencing disruption on sufficiently short time scales. This calculation involves a large ensemble of long-term (~ 100 Myr) solar system integrations and is beyond the scope of this present work. Nonetheless, direct application of equations (3) and (18) suggests that the constraint could be tighter than that derived for the solar system in its usual configuration.

Finally, we note that another class of observational constraints on the solar birth environment might become available. Given that the birth cluster is expected to have $N \approx 10^3 - 10^4$ stars with similar chemical composition, it is possible in principle to find other members of our solar birth aggregate. Although billions of years have passed and the cluster has long since dispersed, perhaps ~ 20 of these solar siblings could reside within 100 pc of the Sun (Portegies Zwart 2009). By focusing on the chemical species that show the most variation from cluster to cluster, it is possible to observationally distinguish these siblings from other stars (Ramírez et al. 2014). The discovery of even a few such stars would provide strong

constraints on the properties of the solar birth cluster and its location within the Galaxy. On the other hand, the Solar System could have had a more complicated dynamical history including large radial migration in the Galaxy (Kaib et al. 2011), which could reduce the chances of finding solar siblings.

6. Conclusion

6.1. Summary of Results

Using results from more than 2 million individual numerical scattering experiments, this paper has found cross sections for the disruption of planetary orbits in solar systems interacting with passing stars and binaries. Our specific results can be summarized as follows:

[1] More compact solar systems have smaller interaction cross sections (Figures 1 and 2). To leading order, the cross section for a given disruption event (e.g., planet ejection or eccentricity increase) scales linearly with the semimajor axis of the initial orbit, i.e., $\langle \sigma \rangle \propto a$ (see Figure 12).

[2] For most systems, the cross section for a given planetary orbit to be disrupted during a scattering encounter is almost independent of the other planets. This feature of the interactions allows for the scaling analysis presented in Section 4. Of course, after the encounter, solar systems that suffer moderate disruption can subsequently experience orbital instability, and this latter effect does depend (quite sensitively) on the other planets in the system. In addition, for highly self-interacting solar systems, those with sufficiently massive planets and/or close orbits, interactions among the planets themselves can lead to effectively higher cross sections (e.g., see Figures 2 and 6).

[3] The dependence of the cross sections $\langle \sigma \rangle$ on the post-encounter eccentricity e has a nearly exponential form (see Figures 1 – 5). As a result, the cross sections can be written $\langle \sigma \rangle \propto \exp[-be]$, where $b \approx 4/3$ provides a good fit across the range of parameter space considered in this work (Figures 13, 14, and 15).

[4] The cross sections depend sensitively on the velocity dispersion $v_{\rm b}$ of the background environment, where the dependence displays a nearly power-law form. Moreover, the shape of the cross section curves, as a function of eccentricity, are nearly the same across the parameter space considered here (Figures 3 and 14). The cross sections can thus be written as $\langle \sigma \rangle \propto v_{\rm b}^{-\gamma} \exp[-be]$, where $\gamma = 7/5$ and $b = 4/3$ provide a good fit over range of interest.

[5] The cross sections depend on the mass M_* of the host star, where the dependence has the approximate form $\langle \sigma \rangle \propto M_*^{-1/3}$. The mass dependence is somewhat more compli-

cated, however, as the cross sections are not fully self-similar (see Figures 4 and 15). For more disruptive encounters (where $e \to 1$ and planets are ejected), the scaling with mass is somewhat steeper and the form $\langle \sigma \rangle \propto M_*^{-1/2}$ provides a better fit (consistent with previous results from Adams et al. 2006).

[6] Most of this work considers planetary orbits with vanishing initial eccentricity e. Nonetheless, for solar systems starting with $e \neq 0$, the interaction cross sections for eccentricity increase are nearly the same (Figure 5), provided that one considers post-encounter eccentricities sufficiently larger than the starting values (roughly, by the increment $\Delta e \sim 0.1$). This finding stands in contrast to the related problem of single stars interacting with binaries, where the cross sections for binaries with $e = 0$ and $e \neq 0$ are significantly different (Heggie & Rasio 1996).

[7] The above results can be combined to write the cross section for solar systems interacting with binaries in the general form

$$\langle \sigma \rangle = 4050 \ (\text{AU})^2 \left(\frac{a}{\text{AU}} \right) \left(\frac{M_*}{M_\odot} \right)^{-1/3} \left(\frac{v_{\text{b}}}{1\text{km/s}} \right)^{-7/5} \exp \left[\frac{4}{3} (1 - e) \right] . \qquad (19)$$

This result holds over the ranges of parameters given by 5 AU $\leq a \leq$ 50 AU, $0.25 M_\odot \leq M_* \leq 2 M_\odot$, 1 km/s $\leq v_{\text{b}} \leq$ 16 km/s, and $0.1 \leq e \leq 1$. Equation (19) is in good agreement with the numerically obtained results: For fixed stellar mass, the RMS relative error for the range of starting semimajor axis, velocity dispersion, and post-encounter eccentricity is less than about 12 percent (see Figures 13 and 14). Including variations in the stellar mass, the RMS error is less than about 20 percent (Figure 15). Over the same regime of parameter space, the cross section itself varies by more than a factor of ~ 1000. Equation (19) provides the total ejection cross sections (including capture events) in the limit $e \to 1$; the cross sections for ejection and capture are listed separately in Table 1.

[8] The cross sections for increasing the spread of inclination angles Δi are comparable to those for increasing eccentricity (Figure 7). The cross sections for Δi also show a nearly self-similar form, and scale with velocity dispersion of the background cluster according to $\langle \sigma \rangle \propto v_{\text{b}}^{-7/5}$ (Figure 16). This scaling exponent is the same as that found for eccentricity increases. The cross sections can be fit with an exponential dependence on the variable $x = \sin \Delta i$. Although inexact, one can identify increases in inclination with increases in eccentricity such that $\Delta x \sim \Delta e$. In general, increases in the spread of inclination angles and orbital eccentricity are well-correlated (Figure 8), although the Δi values for a given e display a wide range. We have also determined the cross sections for increasing the inclination angles beyond $39.2°$, the value required for the Kozai effect to operate (equation [10]).

[9] In addition to the ejection of planets during the scattering encounters, orbital eccen-

tricites can be increased so that planetary orbits will cross each other. Most solar systems in such states will eject — or perhaps accrete — planets on relatively short time scales. For systems with the architecture of the current solar system, the cross section for this channel of secondary ejection is comparable to that of direction ejection, so that the total cross section for ejection is effectively doubled (Figure 9). For the ultra-compact configuration of the solar system (in or near multiple mean motion resonances), the cross section for ejection due to orbit crossing is comparable to that of the standard solar system, but the cross section for direct ejection is smaller.

[10] The cross sections for changing the semimajor axes of the planetary orbits are smaller than those for increasing eccentricity and/or inclination angle (Figure 10). Equivalently, the semimajor axes change much less than the other orbital elements during scattering encounters. In rough terms, 10% changes in the semimajor axis — for planets that remain bound — have approximately the same cross sections as planetary ejection.

[11] The cross sections for solar systems interacting with single stars are smaller than those for binary encounters (Figure 11). The single-star cross sections are nearly self-similar (Figure 17), and scale with the semimajor axis of the planet and cluster velocity dispersion according to $\langle \sigma \rangle \propto a \, v_{\rm b}^{6/5}$. The scaling exponent for velocity is somewhat smaller than that for binaries and the dependence of the cross sections on the post-encounter eccentricity is steeper. On average, the single-star cross sections are smaller than the binary cross sections by a factor of ~ 3.6 for small velocity dispersions ($v_{\rm b} = 1$ km/s). This factor falls to only ~ 2 for larger values $v_{\rm b} \sim 20$ km/s; for higher speeds we expect the binary components to act as two separate stars during the encounters (except for close binaries).

[12] We have briefly revisited the dynamical constraint that can be placed on the birth aggregate of our solar system due to scattering encounters (Section 5). The strength of this constraint depends crucially on whether one assumes that the solar system forms in a robust, long-lived cluster (with $\tau \gtrsim 100$ Myr, like those that become open clusters) or in a short-lived cluster that dissipates within $\tau \sim 10$ Myr. For long-lived clusters, the requirement that the solar system is not disrupted implies an order of magnitude limit on the solar birth aggregate of $N \lesssim 10^4$ (see equation [18]). In practice, one should construct the probability distribution for solar system survival/disruption as a function of N (using the cross sections determined herein), and combine it with the other constraints on the birth cluster (see Figure 7 in Adams 2010; see also Portegies Zwart 2009 and Pfalzner 2013).

[13] The cross section for removing a solar system from mean motion resonance is much higher than that required to disrupt the planetary orbits. For the ultra-compact multi-resonant configuration advocated by some versions of the Nice model, this cross section (see equation [3]) is ~ 9 times larger than the disruption cross section for the usual solar system

architecture. If removal from resonance leads to longer-term instability, then constraints on the solar birth aggregate would be tighter for systems in the multi-resonant configuration.

6.2. Discussion

The cross sections reported in this paper are subject to three different types of uncertainties, and the distinctions among these quantities should be kept in mind. [1] First, the Monte Carlo procedure used to determine specific cross sections (as outlined in Section 2) results in uncertainties due to incomplete sampling. These uncertainties decrease with increasing size of the ensemble of simulations and are proportional to $\mathcal{N}_E^{-1/2}$. Over most of the parameter space, we run sufficient numbers $\mathcal{N}_E$ of scattering experiments so that the sampling errors are less than $\sim 5\%$ and usually even smaller. These sampling errors are present in all of the cross sections presented in Section 3, although they are usually not included on the plots (however, see Figure 5). [2] Next, in Section 4, we explore scaling laws to collapse the cross sections for varying velocity dispersion $v_{\rm b}$, host mass M_*, and planet semimajor axis a into nearly self-similar forms. The range of the resulting scaled functions is thus characterized by the error bars shown in Figures 13, 14, 15, 16, and 17. These error bars represent a measure of the degree to which the cross sections depart from self-similarity. The size of these error bars falls in the range $10 – 15\%$, except for the scaling with the mass of the host star (where the error bars correspond to 20% departures). [3] Finally, the mean of the scaled cross sections are described by fitted functions with simple forms. The differences between these functions and the mean scaled cross sections are of order $5 – 10\%$, smaller than the standard deviations of the different sets of cross sections used to construct the mean forms.

In addition to the uncertainties outlined above, the cross sections calculated herein depend on the features of the stellar population that provides the perturbations. As described in Section 2, the cross sections sample the distributions of stellar masses, binary periods, binary mass ratios, binary orbital eccentricities, etc. Different choices for these distributions will lead to corresponding variations in the cross sections. Although we use observations to specify the distributions, they are nonetheless subject to both measurement error and possible variations from region to region.

The numerical simulations carried out for this paper determine the immediate changes in the orbital elements of the solar systems due to passing stars. However, additional changes in the orbital elements can occur over longer time scales. As one example, after an encounter, a planetary system often has larger eccentricities, which can lead to orbital instability over longer spans of time. But the timescales for such instabilities can have a wide range. For systems where the eccentricities are increased so much that planetary orbits cross, one ex-

pects instability and (usually) planet ejection on a relatively short time. The cross sections for orbit crossing are thus of great interest and are given in Figure 9. For systems with smaller eccenticity increases, however, orbital instability can take much longer. For compact multi-resonant solar systems, modest changes in the orbital elements and/or the removal of the system from its resonant state can lead to instabilities over millions of years (Batygin & Brown 2010). For systems with more widely separated orbits, instabilities can take even longer than the current age of the universe (Batygin & Laughlin 2008; Laskar & Gastineau 2009). To study this issue, the post-encounter solar systems must be integrated over long time scales (up to billions of years) to fully determine the effects of the encounters. This task is left for future work. On another front, the orbits could also damped after the scattering encounters, thereby moving the orbits back towards smaller eccentricities (Levison & Morbidelli 2007; Picogna & Marzari 2014). This effect should also be considered in follow-up studies, especially on time scales of $1 - 100$ Myr when solar systems are expected to retain a significant population of planetesimals.

The scattering encounters considered herein can be effective in sculpting giant planet orbits and the Kuiper Belt of our Solar System (e.g., Kenyon & Bromley 2004). On the other hand, the Oort cloud is too large to be produced within a young embedded cluster (e.g., see Brasser et al. 2012 for further discussion). More specifically, the Oort cloud extends out to $\sim 50,000$ AU (Oort 1950; Jewitt 2001), more than 1000 times the size of the solar systems considered in this paper. With this enormous size, the Oort cloud would be decimated by passing stars within the cluster. As a result, the cloud must be produced later, after the solar system leaves its birth cluster, or perhaps during its exit. Any viable scenario for the solar birth environment must simultaneously account for the Oort cloud, the giant planet orbits, Kuiper Belt properties, radioactive enrichment, Sedna's orbit, and survival of the solar nebula gas reservoir; these coupled constraints thus pose an interesting and challenging opimization problem for further study.

REFERENCES

Adams, F. C. 2010, ARA&A, 48, 47

Adams, F. C., & Fatuzzo, M. 1996, ApJ, 464, 256

Adams, F. C., & Laughlin, G. 2001, Icarus, 150, 151

Adams, F. C., Proszkow, E. M., Fatuzzo, M., & Myers, P. C. 2006, ApJ, 641, 504

Adams, F. C., & Spergel, D. N. 2005, AsBio, 5, 497

Allen, L. et al. 2007, in Protostars & Planets V, ed. B. Reipurth, D. Jewitt, K. Keil, pp. 361–376, (Tucson: Univ. Arizona Press)

Barenblatt, G. I. 2003, Scaling (Cambridge: Cambridge Univ. Press)

Batalha, N. M., Rowe, J. F., Bryson, S. T.. Barclay, T. et al. 2013, ApJS, 204, 24

Battinelli, P., & Capuzzo-Dolcetta, R. 1991, MNRAS, 249, 76

Batygin, K., & Brown, M. E. 2010, ApJ, 716, 1323

Batygin, K., & Laughlin, G. 2008, ApJ, 683, 1207

Batygin, K., & Morbidelli, A. 2013, A&A, 556, 28

Batygin, K., Morbidelli, A., & Tsiganis, K. 2011, A&A, 533, 8

Boley, A. C., Payne, M. J., & Ford, E. B. 2012, ApJ, 754, 57

Brasser, R., Duncan, M. J., Levison, H. F., Schwamb, M. E., & Brown, M. E. 2012, Icarus, 217, 1

Breslau, A., Steinhausen, M., Vincke, K., & Pfalzner, S. 2014, A&A, 565, 130

Cameron, A.G.W., & Truran, J. W. 1977, Icarus, 30, 447

Chabrier, G. 2003, PASP, 115 763

Chatterjee, S., Ford, E. B., Geller, A. M., & Rasio, F. A. 2012, MNRAS, 427, 1587

Craig, J., & Krumholz, M. R. 2013, ApJ, 769, 150

Dauphas, N., & Chaussidon, M. 2011, AREPS, 39, 351

Dukes, D., & Krumholz, M. R. 2012, ApJ, 754, 56

Duquennoy, A., & Mayor, M. 1991, A&A, 248, 485

Fatuzzo, M., & Adams, F. C. 2008, ApJ, 675, 1361

Gomes, R., Levison, H. F., Tsiganis, K., & Morbidelli, A. 2005, Nature, 435, 466

Hao, W., Kouwenhoven, M.B.N., Spurzem, R. 2013, MNRAS, 433, 867

Heggie, D. C., & Rasio, F. A. 1996, MNRAS, 282, 1064

Hillenbrand L. A., & Hartmann L. W., 1998, ApJ, 492, 540

Jewitt, D. J. 2001, ApJ, 123, 1039

Kaib, N. A., Roskar, R., & Quinn, T. 2011, Icarus, 215, 491

Kenyon, S. J., & Bromley, B. C. 2004, Nature, 432, 598

Kozai, Y. 1962, AJ, 67, 591

Kroupa, P., Aarseth, S., & Hurley, J. 2001, MNRAS, 321, 699

Lada, C. J., & Lada, E. A. 2003, ARA&A, 41, 57

Lamers, H.J.G.L.M., Gieles, M., & Portegies Zwart, S. F. 2005, A&A, 429, 173

Laskar, J., & Gastineau, M. 2009, Nature, 459, 817

Laughlin, G., & Adams, F. C. 2000, Icarus, 145, 614

Levison, H. F., & Morbidelli, A. 2007, Icarus, 189, 196

Li, G., & Batygin, K. 2014, submitted to ApJ

Lichtenberg, A. & Lieberman, M. 1992, Regular and Chaotic Dynamics, Applied Mathematical Sciences (New York: Springer)

Lidov, M. L. 1962, Planet. Space Sci., 9, 719

Malmberg, D., Davies, M. B., Heggie, D. C. 2011, MNRAS, 411, 859

Malmberg, D., de Angeli, F., Davies, M. B., Church, R. P., Mackey, D., & Wilkinson, M. I. 2007, MNRAS, 378, 1207

Morbidelli, A., Brasser, R., Tsiganis, K., Gomes, R., & Levison, H. F. 2009, A&A, 507, 1041

Murray, C. D., & Dermott, S. F. 1999, Solar System Dynamics (Cambridge: Cambridge Univ. Press)

Nesvorný, D., & Morbidelli, A. 2012, AJ, 144, 117

Oort, J. 1950, Bull. Astron. Inst. Neth., 11, 91

Pacucci, F., Ferrara, A., & D'Onghia, E. 2013, ApJL, 778, L42

Parker, R. J., & Quanz, S. P. 2012, MNRAS, 419, 2448

Pfalzner, S. 2013, A&A, 549, 82

Picogna, G., & Marzari, F. 2014, A&A, 564, 28

Porras, A., et al. 2003, AJ, 126, 1916

Portegies Zwart, S. F. 2009, ApJL, 696, L13

Press, W. H., Flannery, B. P., Teulkolsky, S. A., & Vetterling, W. T. 1986, Numerical Recipes: The art of scientific computing (Cambridge: Cambridge Univ. Press)

Proszkow, E. M., & Adams, F. C. 2009, ApJS, 185, 486

Ramírez, I., Bajkova, A. T., Bobylev, V. V., Roederer, I. U., Lambert, D. L., Endl, M., Cochran, W. D., MacQueen, P. J., & Wittenmyer, R. A 2014, ApJ, 787, 154

Roberts, M. 1957, PASP, 69, 406

Spurzem, R., Giersz, M., Heggie, D. C., Lin, D.N.C. 2009, ApJ, 697, 458

Thompson, T. A. 2013, MNRAS, 431, 63

Tsiganis, K., Gomes, R., Morbidelli, A., & Levison, H. F. 2005, Nature, 435, 459

Whitmore, B. C., Chandar, R., & Fall, S. M. 2007, AJ, 133, 1067

Williams, J. P. 2010, ConPhy, 51, 381

Williams, J. P., & Gaidos, E. 2007, ApJ, 663, 33

Cross Sections for Ejection and Capture

Configuration	Jupiter	Saturn	Uranus	Neptune
Standard model	15500 ± 1360	34000 ± 2050	72300 ± 3100	113000 ± 3860
	812 ± 306	2140 ± 531	6040 ± 994	11400 ± 1280
Compact model	18100 ± 1510	32700 ± 2130	57500 ± 2790	93900 ± 3570
	915 ± 379	2280 ± 607	4380 ± 817	11500 ± 1320
Resonant model	23900 ± 1810	40200 ± 2440	61100 ± 2990	60100 ± 2900
	1240 ± 467	2150 ± 569	3430 ± 701	3620 ± 738
Massive planets	24100 ± 1890	38300 ± 2390	77700 ± 3360	105000 ± 3880
	1530 ± 579	2170 ± 637	4810 ± 932	8480 ± 1190
$v_b = 2$ km/s	9170 ± 947	14800 ± 1250	29800 ± 1770	45200 ± 2240
	391 ± 136	635 ± 173	2600 ± 487	6370 ± 903
$v_b = 4$ km/s	2980 ± 454	6090 ± 776	10600 ± 918	15700 ± 1140
	270 ± 173	607 ± 230	1580 ± 486	2430 ± 569
$v_b = 8$ km/s	1220 ± 258	2580 ± 403	4060 ± 506	5830 ± 698
	130 ± 85	134 ± 75	239 ± 88	624 ± 228
$v_b = 16$ km/s	181 ± 39	607 ± 113	1220 ± 182	2140 ± 252
	82 ± 52	53 ± 39	214 ± 83	169 ± 69
$M_* = 0.25 M_\odot$	37400 ± 2195	74800 ± 3170	138000 ± 4350	196000 ± 5130
	766 ± 330	3510 ± 742	10300 ± 1240	19500 ± 1720
$M_* = 0.5 M_\odot$	27600 ± 1830	54000 ± 2630	107000 ± 3740	152000 ± 4460
	1730 ± 560	3310 ± 755	7470 ± 1060	15100 ± 1490
$M_* = 2.0 M_\odot$	11000 ± 1170	21700 ± 1720	45700 ± 2420	69300 ± 2980
	458 ± 234	1590 ± 467	4420 ± 844	7410 ± 1110
Single, $v_b = 1$ km/s	3840 ± 651	7100 ± 856	17300 ± 1430	30600 ± 1980
	135 ± 80	587 ± 210	2080 ± 480	5090 ± 871
Single, $v_b = 2$ km/s	1620 ± 324	3110 ± 429	9030 ± 926	13200 ± 1090
	168 ± 86	236 ± 106	1370 ± 423	2810 ± 641
Single, $v_b = 4$ km/s	685 ± 177	1300 ± 244	3740 ± 531	6790 ± 793
	116 ± 94	117 ± 51	360 ± 117	1480 ± 411
Single, $v_b = 8$ km/s	269 ± 103	1090 ± 322	1440 ± 286	1880 ± 266
	21 ± 14	23 ± 14	157 ± 53	374 ± 202

Table 1: For each solar system configuration, as labeled in the left column, the top line lists the ejection cross sections and the second line lists the capture cross sections for each of the planets. The error bars due to incomplete Monte Carlo sampling are included. All cross sections are given in units of AU^2.